REVIEW

www.the-innovation.org

Stable organic radical qubits and their applications in quantum information science

Aimei Zhou,[1,2] Zhecheng Sun,[1,2] and Lei Sun[1,2,3,*]

*Correspondence: sunlei@westlake.edu.cn

Received: March 6, 2024; Accepted: June 20, 2024; Published Online: June 21, 2024; https://doi.org/10.1016/j.xinn.2024.100662

GRAPHICAL ABSTRACT

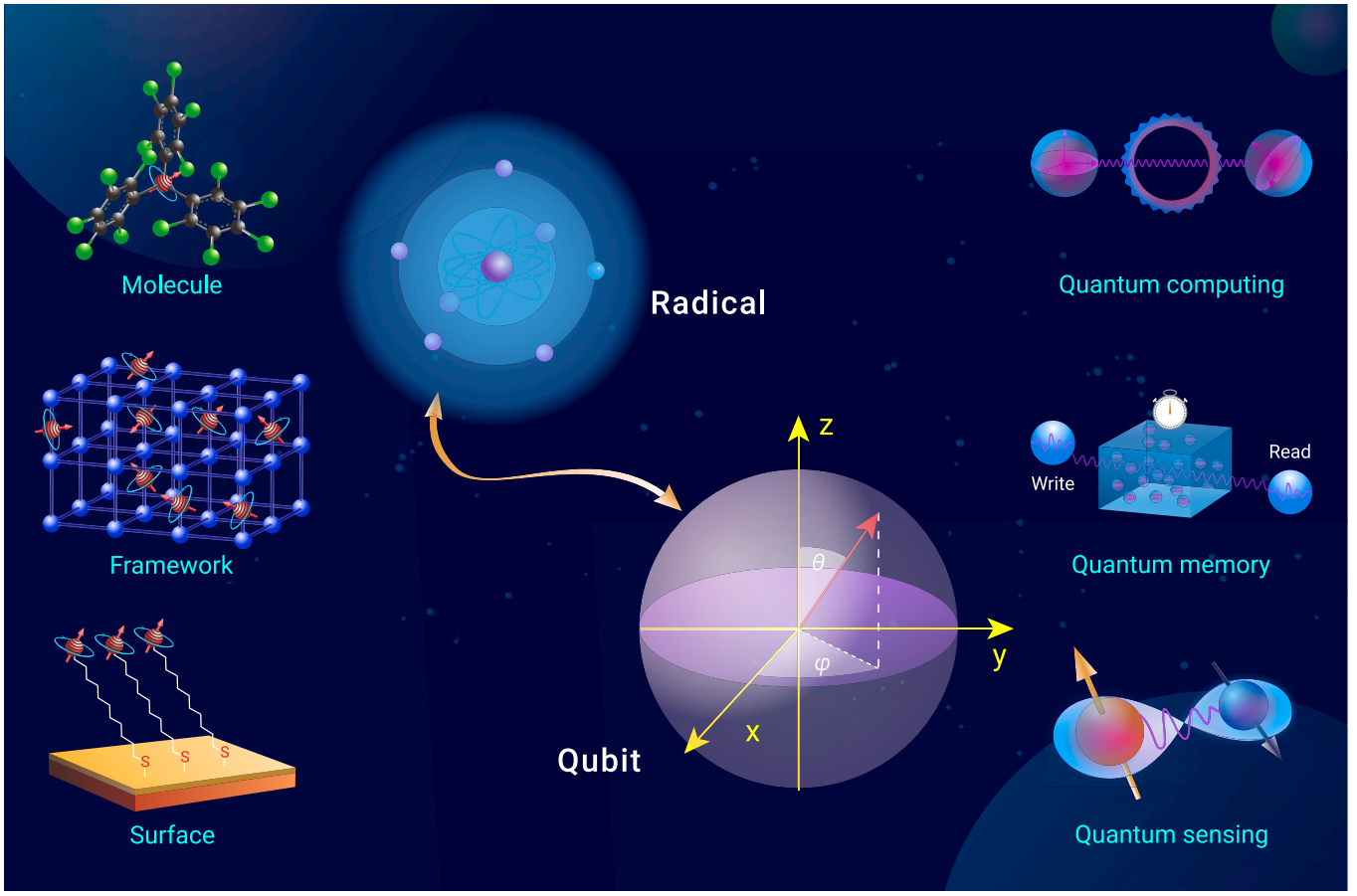

PUBLIC SUMMARY

- Stable organic radicals behave as tunable electron spin qubits with room-temperature quantum coherence.
- Molecular structures, environment, and operation conditions affect electron spin dynamics of radical qubits.
- Radical qubits could be integrated into polymers, microporous frameworks, and thin films.
- Radical qubits enable quantum computing, quantum memory, and quantum sensing.

REVIEW

Stable organic radical qubits and their applications in quantum information science

Aimei Zhou,[1,2] Zhecheng Sun,[1,2] and Lei Sun[1,2,3,*]

[1]Department of Chemistry, School of Science and Research Center for Industries of the Future, Westlake University, Hangzhou 310030, China

[2]Institute of Natural Sciences, Westlake Institute for Advanced Study, Hangzhou 310024, China

[3]Key Laboratory for Quantum Materials of Zhejiang Province, Department of Physics, School of Science, Westlake University, Hangzhou 310030, China

*Correspondence: sunlei@westlake.edu.cn

Received: March 6, 2024; Accepted: June 20, 2024; Published Online: June 21, 2024; https://doi.org/10.1016/j.xinn.2024.100662

Citation: Zhou A., Sun Z., and Sun L. (2024). Stable organic radical qubits and their applications in quantum information science. The Innovation **5(5)**, 100662.

The past century has witnessed the flourishing of organic radical chemistry. Stable organic radicals are highly valuable for quantum technologies thanks to their inherent room temperature quantum coherence, atomic-level designability, and fine tunability. In this comprehensive review, we highlight the potential of stable organic radicals as high-temperature qubits and explore their applications in quantum information science, which remain largely underexplored. Firstly, we summarize known spin dynamic properties of stable organic radicals and examine factors that influence their electron spin relaxation and decoherence times. This examination reveals their design principles and optimal operating conditions. We further discuss their integration in solid-state materials and surface structures, and present their state-of-the-art applications in quantum computing, quantum memory, and quantum sensing. Finally, we analyze the primary challenges associated with stable organic radical qubits and provide tentative insights to future research directions.

INTRODUCTION

Quantum information science (QIS) takes advantage of unique features of quantum mechanics—superposition and entanglement—for information processing, enabling revolutionary technologies including quantum computing, quantum communication, and quantum sensing.[1–4] The development of QIS has led to quantum computers that outperform classical supercomputers in specific tasks,[5,6] eavesdropping-free communication between a satellite and a ground station,[7,8] and *in vivo* metrology of magnetic field and temperature with unprecedented sensitivity and spatial resolution.[9,10] According to the DiVincenzo's criteria, physical implementation of the basic unit of quantum information, i.e., qubit, requires two-level quantum systems that are coherent, initializable, controllable, measurable, and scalable.[11] These criteria have inspired extensive investigations on a myriad of qubit candidates, spanning superconducting circuits,[12] semiconductor quantum dots,[13] trapped ions,[14] neutral atoms,[15] nuclear spins,[16,17] solid-state electron spin defects,[18–20] photons,[2] Majorana zero modes,[21] etc. However, none of them is perfect for all QIS technologies—the physical nature of each candidate determines its applicability and limitation.[22] For instance, superconducting circuits are highly scalable thanks to their compatibility with concurrent semiconductor technologies, making them ideal building blocks for large-scale quantum computers, yet the ultralow operation temperature (tens of millikelvin) restricts their utility in ambient conditions.[12] Therefore, with the growing interests in applying QIS in various scenarios, such as chemical-specific quantum sensing in biological systems, there is a high demand for new types of qubits.

With atomic-level designability and tunability, molecular electron spin qubits, i.e., molecules with unpaired electrons, hold the promise for new opportunities of QIS.[23–27] For instance, chemical-recognizing functional groups can be incorporated for highly selective quantum sensing,[28–30] and multi-level spin states can be engineered to simplify the implementation of quantum algorithms.[31] Recent studies have revealed design principles for molecular electron spin qubits with long-lived quantum coherence,[32] high operating temperature,[33,34] and optical addressability.[35–40] The removal of environmental nuclear spins improves the decoherence time of a vanadium-based coordination complex approaching 1 ms at cryogenic temperature,[32] the suppression of orbital angular momentum gives rise to room temperature coherence of an yttrium-based organometallic molecule,[41] and tailor-designed triplet states enable optical initialization and readout of chromium-based and vanadium-based coordination complexes.[38,42,43] Furthermore, coherent addressing of single-molecular electron spin qubits has been achieved with state-of-the-art single-molecule spectroscopy,[35–37] scanning tunneling microscopy,[44,45] atomic force microscopy,[46] and quantum metrology using a nitrogen-vacancy center in diamond.[47] These advancements have led to prototype demonstrations of molecular QIS technologies, such as a universal two-qubit quantum logic gate with a radical pair,[48,49] quantum error correction with an endohedral fullerene qudit,[31] quantum sensing of ^{1}H and ^{2}H with a Cu^{2+}-containing metal-organic framework (MOF),[50] and intramolecular quantum teleportation with a donor-acceptor molecule.[51] So far, these studies have been focused on coordination complexes[27,52] and photo-generated radicals,[53] which typically suffer from low operating temperature and/or short lifetimes, compromising their applications in ambient conditions. Herein, we sought to revisit stable organic radicals, whose electron spin dynamics has been extensively studied over two decades, yet whose applications in QIS remain underexplored.[54]

Organic radicals are open-shell molecules with one or more unpaired electrons, which generally exhibit short lifetimes and high reactivity.[55] Delocalization and steric hindrance could stabilize organic radicals so that they retain unpaired electrons in ambient conditions.[56,57] Moreover, they could be modified with functional groups to inherit optical,[58,59] electrochemical,[60,61] and magnetic properties,[62] as well as recognition capabilities.[63–65] Their stability and versatile functionalities enable applications in synthesis,[66,67] sensing,[68] optoelectronics,[69] spintronics,[70] and biology.[71] Stable organic radicals also display advantageous spin dynamic properties: they are composed of light elements (C, H, N, O, P, S, etc.) with negligible spin-orbit coupling,[72–74] which give rise to quantum coherence at room temperature and in complex chemical environments. Hence, stable organic radicals have been widely used as spin labels for protein structure determination and as polarizing agents for dynamic nuclear polarization.[75–77]

In this review, we highlight the great potential of stable organic radical qubits in QIS applications (Figure 1), which has attracted little attention so far. Following a summary of known stable organic radical qubits, we introduce their electron spin dynamic properties, i.e., figure of merits of qubit performance, with the emphasis on their mechanisms and optimization strategies. We then summarize trials of integrating stable organic radical qubits into solid-state systems and present prototype applications in various quantum information technologies. Finally, although coordination complexes,[27,52] endohedral fullerenes,[31,78–80] photo-generated radicals,[53,81–83] and injected radicals in devices[84,85] are beyond our scope, we suggest that interested readers explore these alternative molecular qubit systems through additional literature.

STABLE ORGANIC RADICAL QUBITS

Tens of stable organic radicals have been experimentally demonstrated to be qubits, which are summarized in Figures 2 and S1–S4. These include radicals based on triphenylmethyl, nitroxide, semiquinone, and conjugated macrocyclic structural motifs. The triphenylmethyl radical and its derivatives host an electron spin on the central carbon atom, whose stability stems from large steric hindrance and conjugation pathways provided by the surrounding benzene rings.[86] The nitroxide radicals, such as (2,2,6,6-tetramethylpiperidin-1-yl)oxyl (TEMPO), possess an unpaired electron residing on the N-O site and stabilized by delocalization effects.[87,88] o-Phenols and p-phenols can be oxidized to form semiquinone radicals whose electron spins are concentrated on oxygen atoms and stabilized by delocalization.[89] Other radicals, such as tetrathiafulvalene (TTF), 1,3-bisdiphenylene-2-phenylallyl (BDPA), and 2,2-diphenyl-1-picrylhydrazyl, possess unpaired electrons on highly conjugated and sterically hindered

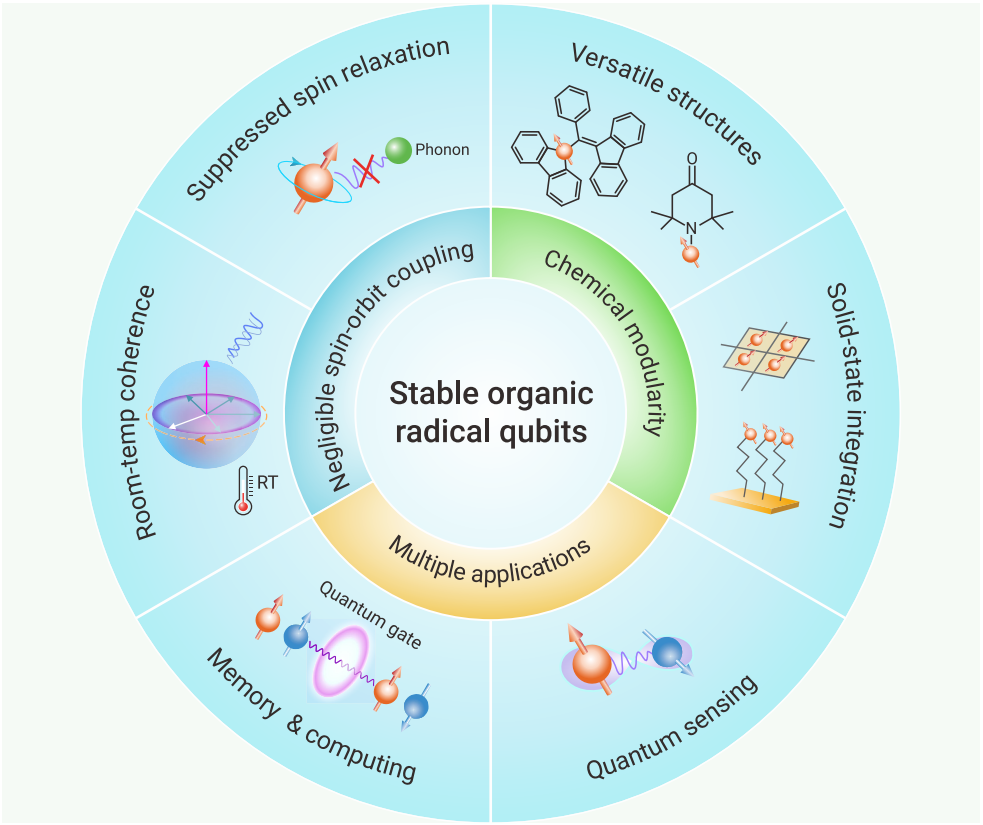

Figure 1. Introduction to stable organic radical qubits

backbones.[90,91] In addition, graphene nanoribbons (GNRs)[92–94] and carbon nanotubes[95] could also host stable radicals via chemical modification. All these stable radicals are potential candidates as qubits as they exhibit decent spin dynamic properties and coherent addressability. In this review, we refer to stable organic radical qubits as radical qubits for simplicity.

ELECTRON SPIN DYNAMICS

QIS applications require qubits to maintain coherence during quantum manipulation and readout.[11] Regarding the radical qubit, this demand translates to long electron spin relaxation time (T_1) and decoherence time (T_2).[23] T_1 describes the time that an electron spin takes to relax from a nonequilibrium state to thermodynamic equilibrium (Figure S5A). T_2 describes the time spanned for the electron spin to lose its phase coherence (Figure S5B). In the literature of radical qubits, T_2 is often referred to as the dephasing time or phase memory time (T_m), which encompasses all dephasing processes. For consistency, we use T_m exclusively in this review. Another criterion of the qubit is the ability to manipulate its quantum state through single-qubit quantum logic gates, i.e., arbitrary rotation on the Bloch sphere (Figure S5C), which could be demonstrated via Rabi oscillations. Both T_1 and T_m need to exceed the duration of a quantum gate operation, which is typically tens of nanoseconds.[54,96] The T_1, T_m, and manipulability of a radical qubit are typically characterized by pulse electron paramagnetic resonance (EPR) spectroscopy with specifically designed microwave pulse sequences (Figure S6; see details in the supplemental information).

The spin relaxation and decoherence mechanisms have been summarized in previous reviews, which are highly recommended to interested readers.[54,96] Here, we briefly introduce core concepts of electron spin dynamics. The spin relaxation is induced by exchanging energy of the spin with environment through spin-spin interaction and spin-lattice coupling. The former, namely the cross-relaxation, takes place through flip-flop of nearby electron spins and nuclear spins. The latter is associated with absorption and/or emission of phonons (lattice vibrations) through various processes including direct, Raman, Orbach, local-mode, thermally activated, and tumbling-dependent processes, which are summarized in Table S1. In the direct process, the spin relaxes by emitting a phonon whose energy is equal to the Zeeman splitting; hence, it is a one-phonon relaxation process. The spin may also undergo two-phonon relaxation, where it transitions to a virtual energy level (Raman process) or a low-lying excited state (Orbach process) by absorbing a phonon and relaxing to its ground state by emitting another phonon. The local-mode process is caused by the localized molecular vibration instead of the lattice vibration. The thermally activated process involves a motion, such as rotation of a methyl group or hydrogen hopping within a hydrogen bond, whose rate is comparable with the Larmor frequency of the spin. Moreover, for molecules in a solution, the tumbling causes spin rotation and modulation of anisotropic interactions, introducing an additional source of relaxation. Finally, electron spins in semiconductors may encounter additional relaxation mechanisms, such as Elliott-Yafet mechanism and D'yakonov-Perel' mechanism, which are beyond the scope of this review.[97]

The spin relaxation induces decoherence as well—T_1 sets the upper limit of T_m with $T_m \leq 2T_1$.[98–100] Nonetheless, in most radicals, the decoherence is mainly caused by environmental magnetic noise that modifies Larmor frequencies of electron spins and accordingly reduces the phase coherence of their quantum states. Such a decoherence effect manifests itself in two types of processes: instantaneous diffusion and spectral diffusion.[54,96] The instantaneous diffusion takes place if the electron spin of interest and a nearby electron spin display similar Larmor frequencies. In this case, applying a resonant pulse simultaneously rotates both spins. The rotation of the latter instantaneously alters the magnetic field experienced by the former, which causes decoherence. The spectral diffusion is caused by nuclear spins, electron spins, and rotary functional groups (e.g., methyl and phenyl groups), etc. These species may introduce stochastic magnetic noise that leads to decoherence of the electron spin of interest during the free evolution time. In addition, for electron spins with anisotropic *g*-factors or anisotropic hyperfine interactions, molecular tumbling in solution effectively acts as magnetic noise by modulating the anisotropy, thus it also results in decoherence.[54,96]

In Tables 1 and S2, we have compiled a summary of experimentally demonstrated radical qubits, along with their corresponding spin dynamic properties, to the best of our knowledge. The majority of radical qubits exhibit coherence at room temperature with T_1 consistently surpassing T_m. At room temperature, most radicals exhibit T_1 values on the order of tens of microseconds, whereas their T_m values are mostly on the order of microseconds or hundreds of nanoseconds. Notably, several radicals based on GNRs could display exceptionally long T_1 at room temperature, approaching nearly 1 ms when dissolved in d_{14}-*o*-terphenyl.[92,93] Moreover, identical radical qubits may display remarkably different values for T_1 and T_m when characterized under different conditions. Even under the same condition, subtle adjustments to the structure of radicals and choice of solvents can induce significant variations. Therefore, spin relaxation and decoherence processes of a radical qubit could be tweaked by molecular design and environmental engineering. Herein, we discuss the influence of molecular structure, temperature, solvent, Larmor frequency, radical concentration, and pulse sequence on the spin relaxation and decoherence processes, aiming at providing a framework of designing radical qubits and interpreting their spin dynamic properties.

Molecular structure

The structure of a molecule determines intrinsic properties of its electron spin (*g*-anisotropy, spin multiplicity, etc.), contributes to the phononic and magnetic environment, and dictates their interactions. The spin relaxation is mainly affected by spin-orbit coupling and molecular rigidity.[99] A strong spin-orbit coupling facilitates spin relaxation because it allows the motion of an electron

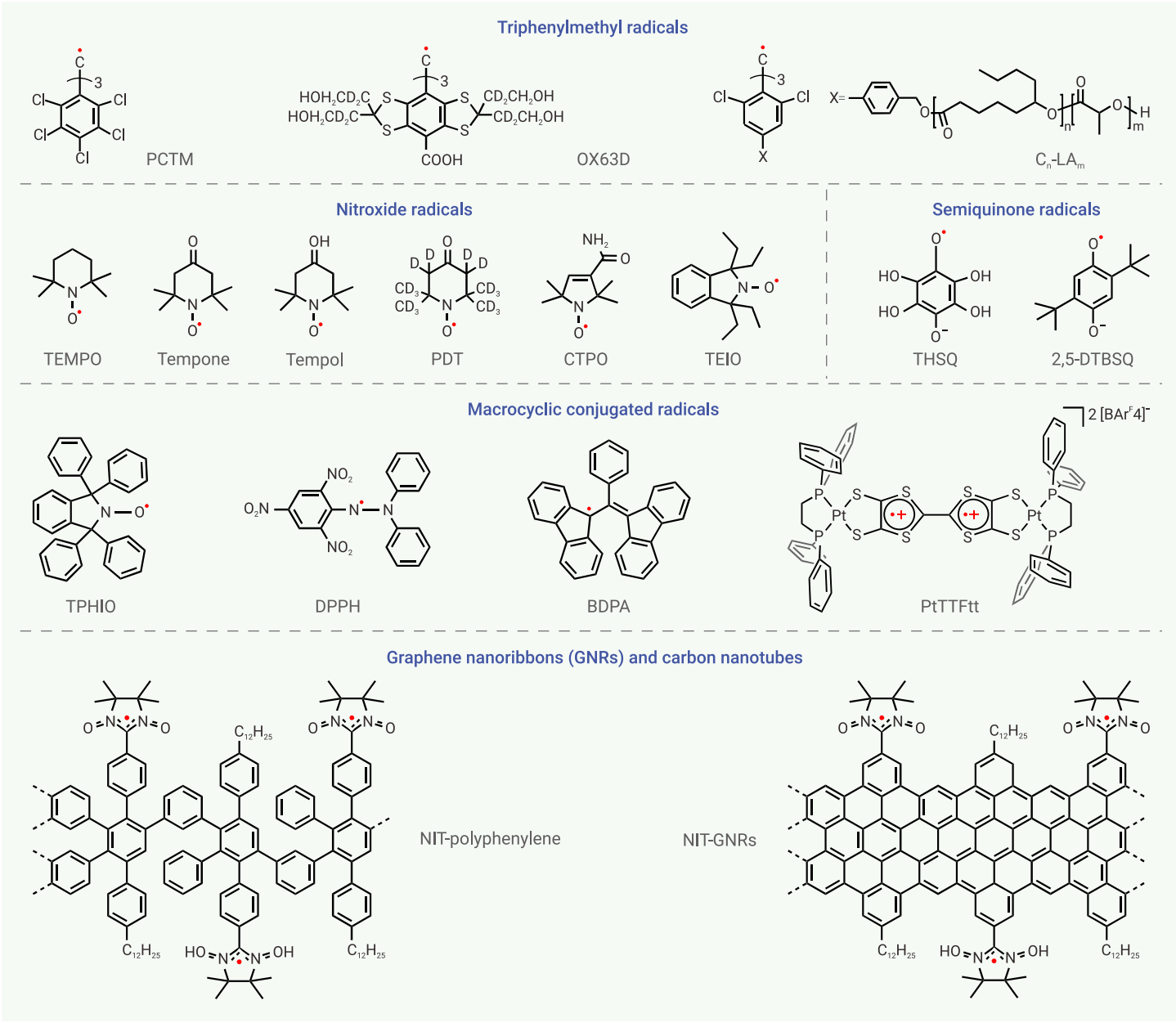

Figure 2. Schemes of selected stable organic radical qubits

(e.g., vibration) to affect its spin state (Figure 3B). It also gives rise to *g*-anisotropy that intensifies the tumbling-induced relaxation in solution (Figure 3A).[117] As the strength of spin-orbit coupling decreases with decreasing atomic number, radical qubits that consist of only light elements exhibit weak spin-orbit coupling and in turn suppressed spin relaxation.[72–74] Therefore, they could maintain microsecond-scale T_1 even at room temperature (Tables 1 and S2), which is difficult for metal-based molecular qubits with only a few exceptions.[33,34,41,118–120] Another strategy to slow down spin relaxation is to reduce the density of states of low-frequency phonons that couple strongly to the electron spin.[121–128] This often translates to a rigid structure enforced by conjugation and steric hindrance. For instance, improving the degree of conjugation of and introducing bulky groups into nitroxide radicals consistently increase T_1 across a wide range of temperature (Figure 3D),[107] and incorporating radicals onto GNRs, i.e., hydrocarbons with extended conjugation, gives rise to T_1 up to 1 s at 5 K.[92,93]

The major sources of electron spin decoherence are nearby nuclear spins.[96] The influence of a nuclear spin depends on its distance from the electron spin and its magnetic moment. When the nuclear spin resides within a certain radius (typically 4–8 Å depending on the magnetic moment) of the electron spin, a distance called the spin-diffusion barrier, they are strongly coupled by hyperfine/superhyperfine interactions (Figure 3C).[96,131,132] This detunes the nuclear spin to other more distant nuclei in the bath, reducing its participation in nuclear flip-flop events. As a result, the nuclear spin within the spin-diffusion barrier exerts little contribution to decoherence. In contrast, when the nuclear spin is beyond the spin-diffusion barrier, it tends to reduce T_m of the electron spin and its decoherence effect scales with the magnetic moment.[131] Therefore, a useful design strategy for improving coherence is to reduce the number of nuclear spins beyond the spin-diffusion barrier. For radicals that can rarely avoid hydrogen atoms, deuteration could significantly improve T_m because ^{2}H has a much smaller magnetic moment than ^{1}H. Besides ^{2}H, ^{35}Cl and ^{37}Cl have low nuclear gyromagnetic ratios, offering viable alternatives to ^{1}H for extending T_m. For instance, substituting chlorine for hydrogen onto aromatic rings of the triphenylmethyl radical significantly enhances its T_m as showcased in the recent investigation by Dai et al. (Figure 3E).[114] Besides nuclear spins, motions of functional groups, e.g., rotation of methyl groups and liberation of phenyl groups, could also generate magnetic noise that causes decoherence.[54] Zecevic et al. systematically examined the impact of methyl groups on the T_m of the tempone radical. They deliberately mixed various solvents to maintain a relatively constant total proton concentration while tuning the ratio of methyl to non-methyl protons. They observed that an elevated concentration of methyl protons expedites

Table 1. T_1 and T_m of selected stable organic radical qubits

Radical[a]	Concentration / mmol·L^{-1}	Frequency / GHz	Solvent	Temperature / K	T_1 / μs	T_m / μs	Reference
OX63D	1	9.5	H_2O: glycerol = 4:6	77	3334[a]	NA[b]	Chen et al.[101]
		95			5000[a]		
OX63D	NA[b]	9.5	MeOH	300	16.5	5.8	Kuzhelev et al.[102]
		34			15.6	1.8	
OX63D	NA[b]	9.5	H_2O	300	16.0	7.3	Kuzhelev et al.[102]
		34			15.3	2.2	
OX63D	NA[b]	9.5	D_2O	300	16.1	7.6	Kuzhelev et al.[102]
		34			16.1	2.0	
OX63D	NA[b]	9.5	$CHCl_3$	300	11.4	9.1	Kuzhelev et al.[102]
		34			11.2	5.4	
BDPA	0.0007	9.5	Toluene	Ambient	12[c]	9.8[c]	Meyer et al.[103]
DPPH	0.012	9.5	Toluene	Ambient	2.0[c]	1.3[c]	Meyer et al.[103]
PDT	0.25	9.5	H_2O	Ambient	0.56	0.59	Meyer et al.[103]
2,5-DTBSQ	0.3	9.5	Ethanol	Ambient	7.8[c]	3.2[c]	Elajaili et al.[104]
TEMPO	1.0	9.5	H_2O: glycerol = 1:1	295[a]	2.00[c]	NA[b]	Sato et al.[105]
Tempone	0.3	9.5	H_2O: glycerol = 1:1	100	100[c]	5[c]	Nakagawa et al.[106]
Tempol	3	9.5	Sucrose octaacetate	298[a]	19.95[c]	NA[b]	Sato et al.[107]
DTBN	3	9.5	Sucrose octaacetate	250[a]	5.6[c]	0.40[c]	Sato et al.[107]
TEIO	3	9.5	Sucrose octaacetate	300[a]	25.12[c]	0.63[c]	Sato et al.[107]
PCTM	0.2-0.5	9.5	Toluene : $CHCl_3$ = 4:1	298	10[c]	NA[b]	Kathirvelu et al.[108]
PtTTFtt	0.05	9.5	DCM	298	1.44[c]	0.34[c]	McNamara et al.[109]
NIT-polyphenylene	NA[b]	9.4	Powder	300[a]	1.43[c]	0.6[c]	Slota et al.[92]
NIT-GNRs	NA[b]	9.4	Powder	300[a]	1.43[c]	0.2[c]	Slota et al.[92]
C_{50}-LA_{90}	1%[d,e]	9.73	NA[b]	30	2102	0.186	Hou et al.[110]
		9.65		298	25.02	0.148	
C_{50}-LA_{140}	0.7%[d,e]	9.73	NA[b]	30	3522	0.300	Hou et al.[110]
		9.65		298	29.62	0.213	
C_{50}-LA_{400}	0.4%[d,e]	9.73	NA[b]	30	5173	0.377	Hou et al.[110]
		9.65		298	29.23	0.318	
MgHOTP	0.66%[e]	9.4	NA[b]	296	10.55	0.153	Sun et al.[111]
				296	21.61[f]	0.202[f]	
TAPPy-NDI	0.01%[e]	9.4	NA[b]	100	790	1.26	Oanta et al.[112]
				296	30.2	0.49	
Ni-HATI_iPr	1%[e]	9.7	NA[b]	100	3[c]	0.09[c]	Lu et al.[113]
PTCM	0.1%[e]	9.26	NA[b]	100	150[c]	1.5[c]	Dai et al.[114]
				298	35.6	1.08	
TEMPO SAM	NA[b]	9.47	NA[b]	10	9200	13.53	Tesi et al.[115]
BTEV-BTR	1%[e]	9	NA[b]	80	386	4.39	Poryvaev et al.[116]

See the full collection of data in Table S2.
[a]Abbreviations are consistent with those in Figures S1-S4.
[b]Not available.
[c]Value estimated from a figure in the reference.
[d]value estimated from the synthetic condition.
[e]Molar percentage of the radical.
[f]MgHOTP soaked in THF.

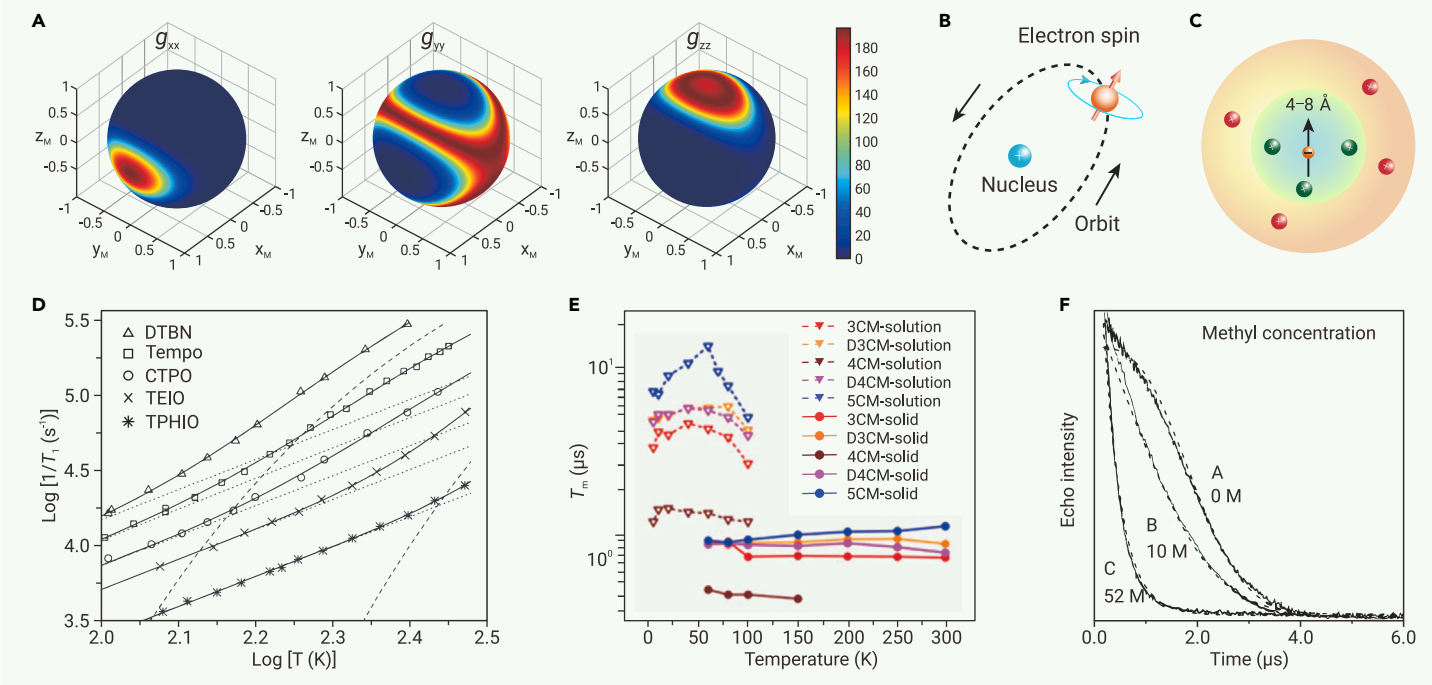

Figure 3. Influence of molecular structures on spin dynamics (A) *g*-Anisotropy mapped on a Bloch sphere calculated with EasySpin.[129] (B) Illustration of spin-orbit coupling. (C) Illustration of spin diffusion barrier (inner circle). Green nuclei are within the spin diffusion barrier, and the red ones are out of it. (D) Influence of conjugation and steric hindrance on T_1 of various nitroxide radicals dissolved in sucrose octaacetate. Dotted and dashed lines represent contributions from the Raman process and thermally activated process, respectively, and solid lines represent their sums. Reproduced from Sato et al.[107] with permission from Taylor & Francis, copyright 2007. (E) Influence of the number of chlorine atoms substituted on triphenylmethyl radicals on their T_m values. The triphenylmethyl radical was either dissolved in d_8-toluene solution or diluted in powders of hydrogenated diamagnetic analogues. 5CM is the same as PCTM (Figure 2). Reproduced from Dai et al.[114] with permission from John Wiley & Sons, copyright 2018. (F) Influence of concentration of methyl groups in solution on the T_m of tempone radical. Reproduced from Zecevic et al.[130] with permission from Taylor & Francis, copyright 1998.

decoherence (Figure 3F).[130] Thus, it is advised to avoid rotary groups through molecular design to improve T_m.

Temperature

Temperature affects the harmonicity and excitation of phonon modes of a radical, which in turn influences its spin-lattice coupling. Depending on the coupling mechanism, spin relaxation processes exhibit different temperature dependencies (Figure 4A; Table S1) and dominate in different temperature regions. Cross-relaxation is typically temperature independent.[133,134] The direct relaxation rate ($1/T_1$) is linear to temperature and is typically salient at low temperatures (mostly below 10 K). The Raman process is significant at higher temperature. Its relaxation rate often exhibits exponential dependence on temperature.[135,136] The exponent may be 7–9 if only acoustic phonons are involved in spin-lattice coupling and may appear as 3–5 if optical phonons are involved as well. Moreover, the exponent is close to 2 in the high-temperature limit where the thermal energy well exceeds the energies of phonons participating in spin-lattice coupling. At even higher temperature, thermally activated and local-mode processes may dominate the spin relaxation. The thermally activated relaxation rate levels off when the thermal energy is well above the activation energy, whereas the local-mode processes become faster as temperature increases. The relaxation rate of the Orbach process also increases with increasing temperature, and its contribution is especially significant when the thermal energy exceeds the excitation energy. In addition, in fluid solutions, the tumbling process is typically dominant, and the temperature dependence of the tumbling relaxation rate is correlated to that of the solvent viscosity, which is discussed in the next sub-section.[54,96]

Fitting the temperature dependence of T_1 with the formulae summarized in Table S1 could reveal processes involved in spin relaxation at certain temperature, and it can offer valuable insights into spin dynamics, including spin-phonon coupling strengths, Debye temperatures, activation energies of specific intramolecular motions, molecular vibrations strongly coupled to the spin, and low-lying excited spin states, among other factors. For instance, fitting the T_1 of d_{24}-OX063 collected at 5–100 K with the above-mentioned spin relaxation mechanisms shows that the direct process dominates below 10 K, whereas the Raman and Orbach processes play major roles above 10 K (Figure 4C).[101] The fitting further revealed the Debye temperature of 135 K and an excitation energy of 0.3 meV. This information is critical to understand the spin dynamics of this radical and its performance in dynamic nuclear polarization. Similarly, in polyphenylene and GNR modified by nitronyl nitroxide radicals (NIT-polyphenylene and NIT-GNR, respectively), fitting variable-temperature T_1 reveals direct, Raman, and local mode processes dominating below 25 K, between 25 and 200 K, and above 200 K, respectively (Figure 4D).[92] The local mode process is associated with a characteristic energy of 1,354 cm^{-1}, which indicates a dominant contribution from the stretch of the N-O bond to the spin relaxation.

The temperature dependence of T_m is mainly determined by nuclear spin diffusion, motional effects, molecular tumbling processes, and spin relaxation.[54,96] They dominate at different temperature regions. At low temperature, intramolecular motions are quenched, solvent is frozen, and spin relaxation is slow, so the decoherence is mainly caused by nuclear spin diffusion. T_m is independent of temperature in this regime, which has been observed in trityl-CH_3 and trityl-CD_3 radicals.[137] As temperature increases, motions, e.g., rotation of methyl groups, become active, which causes decoherence and significantly reduces T_m. In frozen solutions, as the temperature approaches the glass transition temperature of the solvent, the complex motion of the solvent molecules can shorten the T_m strongly to make coherence undetectable. In contrast, when the temperature further increases well above the solvent's melting point, the rapid molecular tumbling tends to average out the *g*-anisotropy and mitigate the impact of the surrounding environment, leading to an increase in T_m with increasing temperature. Finally, in both fluid solution and solid state, T_1 becomes short at high temperature, providing the upper limit of T_m. These temperature dependencies of T_m manifest themselves in two TTF-based coordination complexes, mono-radicaloid PtTTFtt+ and diradicaloid PtTTFtt, dissolved in a mixture of dichloromethane and toluene.[109] The T_m of each complex exhibits a small variation within the temperature range of 20–90 K, declines sharply as the temperature further increases, and becomes unmeasurable at 130–220 K (melting points of toluene and dichloromethane are 178.1 and 176.5 K, respectively). Above 220 K, where the solution is fluid, T_m increases with increasing temperature (Figure 4B).

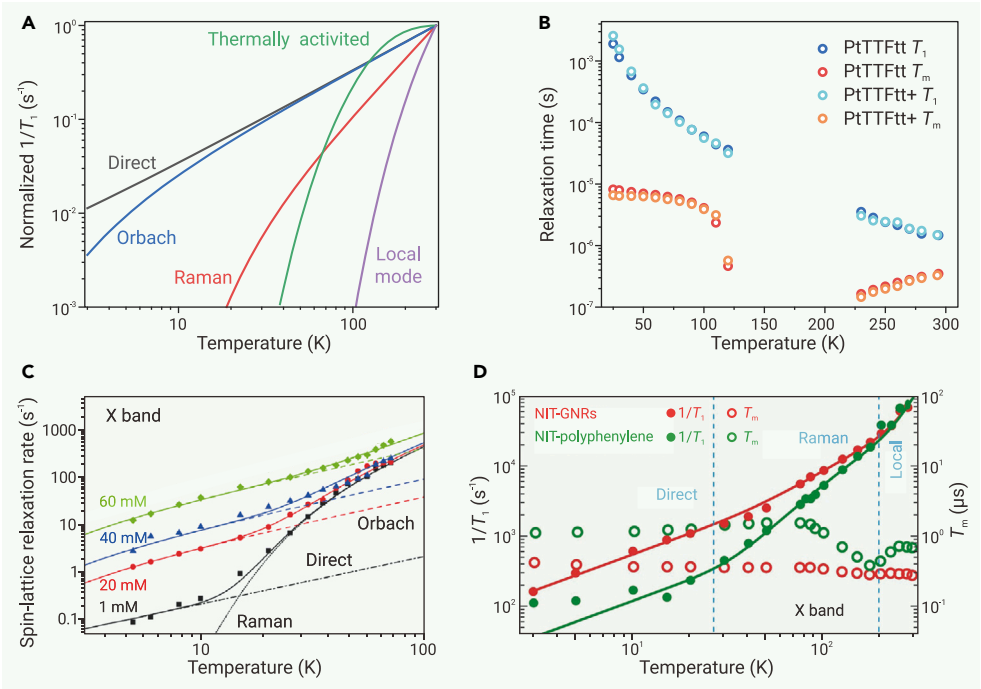

Figure 4. Influence of temperature on spin dynamics
(A) Temperature dependence of spin-lattice relaxation rate under various relaxation processes normalized to the $1/T_1$ at 300 K. Simulations were performed based on corresponding equations in Table S1, and simulation parameters of Orbach, Raman, thermally activated, and local-mode processes are arbitrary. (B) Temperature dependence of T_1 and T_m for PtTTFtt and PtTTFtt+. Reproduced from McNamara et al.[109] ©The Authors, some rights reserved; distributed under CC-BY-NC-ND 4.0 (http://creativecommons.org/licenses/by-nc-nd/4.0/). (C) Temperature dependence of spin-lattice relaxation rate for d_{24}-OX063 with various concentrations. Reproduced from Chen et al.[101] with permission from Royal Society of Chemistry, copyright 2016. (D) Temperature dependence of $1/T_1$ and T_m for NIT-GNRs and NIT-polyphenylene. Reproduced from Slota et al.[92] with permission from Springer Nature, copyright 2018.

Solvent and Larmor frequency

The impact of solvent on spin relaxation mainly stems from its viscosity and protons (hydrogen atoms). In fluid solution, spin relaxation processes mainly include tumbling-induced spin rotation and modulation of anisotropic interactions comprising *g*-anisotropy, *A*-anisotropy, and dipolar coupling with solvent nuclei (Figures 5A–5D).[54] An increase in viscosity enhances collisions between spin centers and solvent molecules, intensifying the effects of *g*-anisotropy and *A*-anisotropy that reduce T_1 and T_m. In addition, the tumbling correlation time, τ_R, increases with increasing viscosity, which may alter the spin relaxation mechanism as well as the dependence of T_1 on the Larmor frequency of electron spin (ω).[138] As exemplified in solutions of the PDT radical,[117] when $(\omega\tau_R)^2 \ll 1$, the tumbling is fast, which effectively averages out the *g*-anisotropy and *A*-anisotropy, rendering the spin system isotropic. As a result, T_1 is governed by the spin rotation that is frequency independent. When $(\omega\tau_R)^2$ is non-negligible, the modulation of anisotropic interaction is significant, and T_1 becomes frequency dependent—T_1 increases with increasing ω. (The frequency dependencies of T_1 and T_m remain underexplored likely due to limited availability of multi-band EPR spectrometers; see further discussions in the supplemental information.).

Protons in solvent molecules typically facilitate spin relaxation and decoherence. Their nuclear spins act as environmental magnetic noise that weakly couples to electron spins through superhyperfine interaction, reducing both T_1 and T_m via spectral diffusion. Deuteration helps relieve this problem because the nuclear magnetic moment of deuterium is six times less than that of the proton. For instance, at 250 MHz and room temperature, the trityl-CD_3 exhibits T_1 and T_m of 12.2 and 11 μs in H_2O, respectively, while these values become 16.4 and 14 μs in D_2O.[138] Furthermore, N- and O-based radicals readily form hydrogen bonds with protons of polar solvent molecules, which facilitates spin relaxation through proton hopping within the hydrogen bonds, a thermally activated process. This phenomenon is evident in the study on semiquinone radicals dissolved in alcoholic solvent.[54,96] Replacing OH with OD in the solvent approximately halves the relaxation rate.[104] Complete deuteration of the solvent further improves T_1 and almost eliminates its frequency dependence, indicating that thermally activated proton hopping dominates spin relaxation in this system (Figure S7).

Radical concentration

The radical concentration determines spin-spin interaction, which induces both spin relaxation and decoherence. For a radical in solution, its concentration dependence of T_1 depends on the charge state. T_1 of a positively or negatively charged radical remains concentration independent at relatively high concentration because the radicals tend to repel each other to keep long spin-spin distance and in turn weak spin-spin interaction. For instance, semiquinone radicals, which hold negative charges, exhibit negligible concentration dependence of T_1 up to 1 mmol/L.[140,141] In contrast, neutral radicals, e.g., nitroxide radicals, lack Coulombic repulsion and could get close to each other transiently, leading to strong dipolar interaction and significant concentration dependence of T_1. On the other hand, the influence of charge is not salient for radicals in solids where they cannot easily move, as exemplified by radicals embedded in a covalent organic framework (COF).[112]

The rate of instantaneous diffusion linearly scales with the radical concentration, so the T_m decreases with increasing radical concentration, as exemplified by tempol.[142] When the radical concentration is high, instantaneous diffusion dominates the spin decoherence.[54,96] As a result, the influences of nuclear spin diffusion and motional groups are not salient, and T_m tends to be temperature independent. At low radical concentration, instantaneous diffusion is suppressed, nuclear modulations of the electron spin precession become significant, and T_m shows temperature dependence. Because spin-spin interaction induces severe decoherence, it is necessary to dilute the radical to achieve a long T_m.

Pulse sequence

A pulse sequence can be considered as a noise filter that partially eliminates environmental noise.[143] As both T_1 and T_m are sensitive to such noise, they are dependent on pulse sequences used for their characterization. T_1 is typically characterized by saturation recovery and inversion recovery pulse sequences (Figure S6). Saturation recovery involves applying either a strong, long pulse or a series of π/2 pulses, known as a "picket fence," to achieve saturation, resulting in the equal partition of spins between the ground state and the excited state. The long time of this saturation process effectively averages out the influence of spectral diffusion, so this pulse sequence approaches the intrinsic T_1.[142,144] In contrast, the inversion recovery uses a short π pulse to flip the spin to its excited state, so it is prone to spectral diffusion and usually gives rise to shorter T_1 compared with that acquired by the saturation recovery—$T_1^{IR} < T_1^{SR}$.[145]

T_m could be measured by free induction decay (FID) as well as Hahn echo decay, Carr-Purcell-Meiboom-Gill (CPMG), and more advanced dynamical decoupling pulse sequences. The FID reflects the decoherence effect encompassing all influencing factors.[142] The Hahn echo decay pulse sequence exerts a refocusing π pulse (Figure S6) that suppresses the decoherence caused by static non-uniformity in the magnetic environment, but it is difficult to completely eliminate spectral diffusion because a single π pulse gives rise to a wide noise window.[54] The CPMG pulse sequence applies a train of spin-locking π pulses that further suppresses spectral diffusion and improve coherence by filtering out environmental noise efficiently.[146–149] Thus, T_m generally increases with an increasing number of π pulses applied—$T_m^{FID} < T_m^{Hahn} < T_m^{CPMG}$ (Figure 5E).[139] For example, for radicals trapped on chemically modified carbon nanotubes, Hahn echo gives rise to a T_m = 1.2 μs at 5 K, whereas CPMG significantly improves T_m, reaching 8.2 μs with 32 π pulses (Figure 5F).[95] Sometimes, a long CPMG pulse sequence could improve T_m toward T_1.[146]

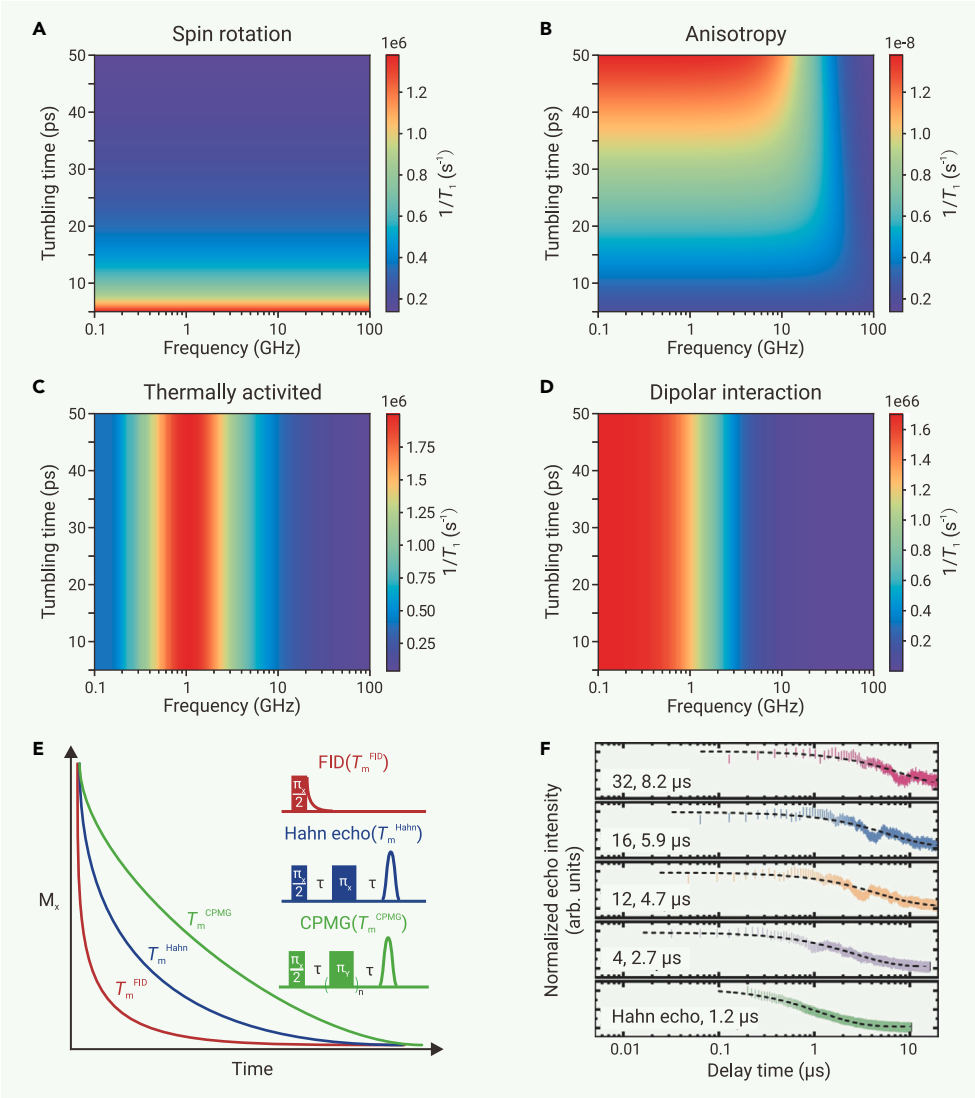

Figure 5. Influence of Larmor frequency and pulse sequence on spin dynamics (A–D) Spin relaxation driven by (A) spin rotation, (B) modulation of *g*-anisotropy and *A*-anisotropy, (C) thermally activated process, and (D) dipolar interaction, respectively, with solvent nuclei under various tumbling times and Larmor frequencies. Simulations were performed based on the corresponding equations in Table S1, and simulation parameters are arbitrary. (E) FID, Hahn echo, and CPMG decay curves. Reproduced from Mirzoyan et al.[139] with permission from John Wiley & Sons, copyright 2021. (F) Echo decay curves acquired by Hahn echo or CPMG sequences with various numbers of π_Y pulses for chemically modified carbon nanotubes. Reproduced from Chen et al.[95]; distributed under CC-BY 4.0 (http://creativecommons.org/licenses/by/4.0/).

In addition, the pulse itself could also influence T_1 and T_m. First, instrumental artifacts, e.g., the instability and imprecision of the microwave source and amplifier as well as the pulse generator, could introduce pulse errors that cause relaxation and decoherence and shorten both T_1 and T_m. As pulse errors accumulate with an increasing number of pulses, the abovementioned coherence enhancement of the CPMG pulse sequence tends to saturate at a certain sequence length. More advanced dynamical decoupling sequences, such as XY8, could be applied to eliminate pulse errors and improve T_m.[150–152] Second, given a certain spin rotation angle, a longer pulse shows a narrower excitation bandwidth that excludes more environmental noise. Thus, the long pulse tends to improve both T_1 and T_m.[153,154] Similarly, as the pulse shape also influences the excitation bandwidth, e.g., a chirped pulse exhibits much wider excitation bandwidth than a rectangular pulse, it should alter T_1 and T_m as well.[155]

Overall, the experimentally observed T_1 and T_m values are highly influenced by the methods used for their characterization. Therefore, when acquiring the spin dynamics of even the same spin system at various conditions (temperature, radical concentration, etc.), it is necessary to maintain consistent pulse sequences and pulse parameters to ensure comparability.

Guidelines for improving T_1 and T_m

The above discussions point out the following guidelines for improving T_1 and T_m of radical qubits through optimization of molecular structures, environmental conditions, and operational parameters.

a) *Improve structural rigidity*: a rigid structure reduces low-energy phonons/vibrational modes, thereby enhancing T_1. The structural rigidity can be designed by introducing steric hindrance and conjugation.

b) *Eliminate nuclear spins*: nuclear spin diffusion is the major source of decoherence at low temperature, so reducing the number of surrounding nuclear spins improves T_m. The most efficient strategy is to construct radical qubits with nearly nuclear-spin-free elements including C, O, and S. If hydrogen atoms are unavoidable, they should be positioned within the nuclear spin diffusion barrier or be replaced by deuterium or chlorine atoms. Similarly, the solvent should also be free of nuclear spins (e.g., CS_2) or be deuterated.

c) *Avoid rotary groups*: rotary groups such as methyl, phenyl, and amino groups act as environmental magnetic noise that reduces both T_1 and T_m. They should be eliminated from the radical by molecular design and from the solvent by avoiding toluene, *N*,*N*-dimethylformamide, dimethyl sulfoxide, acetonitrile, etc.

d) *Reduce temperature*: low temperature helps improve both T_1 and T_m. This is viable for quantum computing and quantum memory but may not be feasible for quantum sensing that ideally operates at room temperature.

e) *Reduce radical concentration*: spin-spin interaction causes instantaneous diffusion that facilitates both spin relaxation and decoherence. Therefore, given sufficient spins for EPR detection, the radical concentration should be as low as possible to improve T_1 and T_m.

f) *Use long pulses*: a long pulse helps improve both T_1 and T_m. Practically, as the spin loses coherence during the pulse, the pulse length should be much shorter than the T_m.

g) *Apply dynamical decoupling*: dynamical decoupling pulse sequences could eliminate spectral diffusion, instantaneous diffusion, and decoherence caused by pulse errors, so they can greatly improve T_m.

SOLID-STATE INTEGRATION

Integration of radical qubits into solid-state materials and architectures can combine qubit behaviors with versatile functionalities and processabilities, opening the possibility of integrating QIS with well-established technologies, such as organic electronics, spintronics, optoelectronics, and chemical sensing. Although there have been extensive studies on polymers,[156,157] COFs,[158,159] MOFs,[160–162] thin films,[163–165] self-assembled monolayers (SAMs),[166–168] and functionalized nanoparticles[116] consisting of stable organic radicals, the spin dynamics in these solid-state structures has rarely been investigated. Compared with small molecules, polymers and framework materials have soft backbones and modular structures. These characteristics impart tunable phonon modes and designable spatial distribution of radicals,[169–171] thereby creating additional platforms to

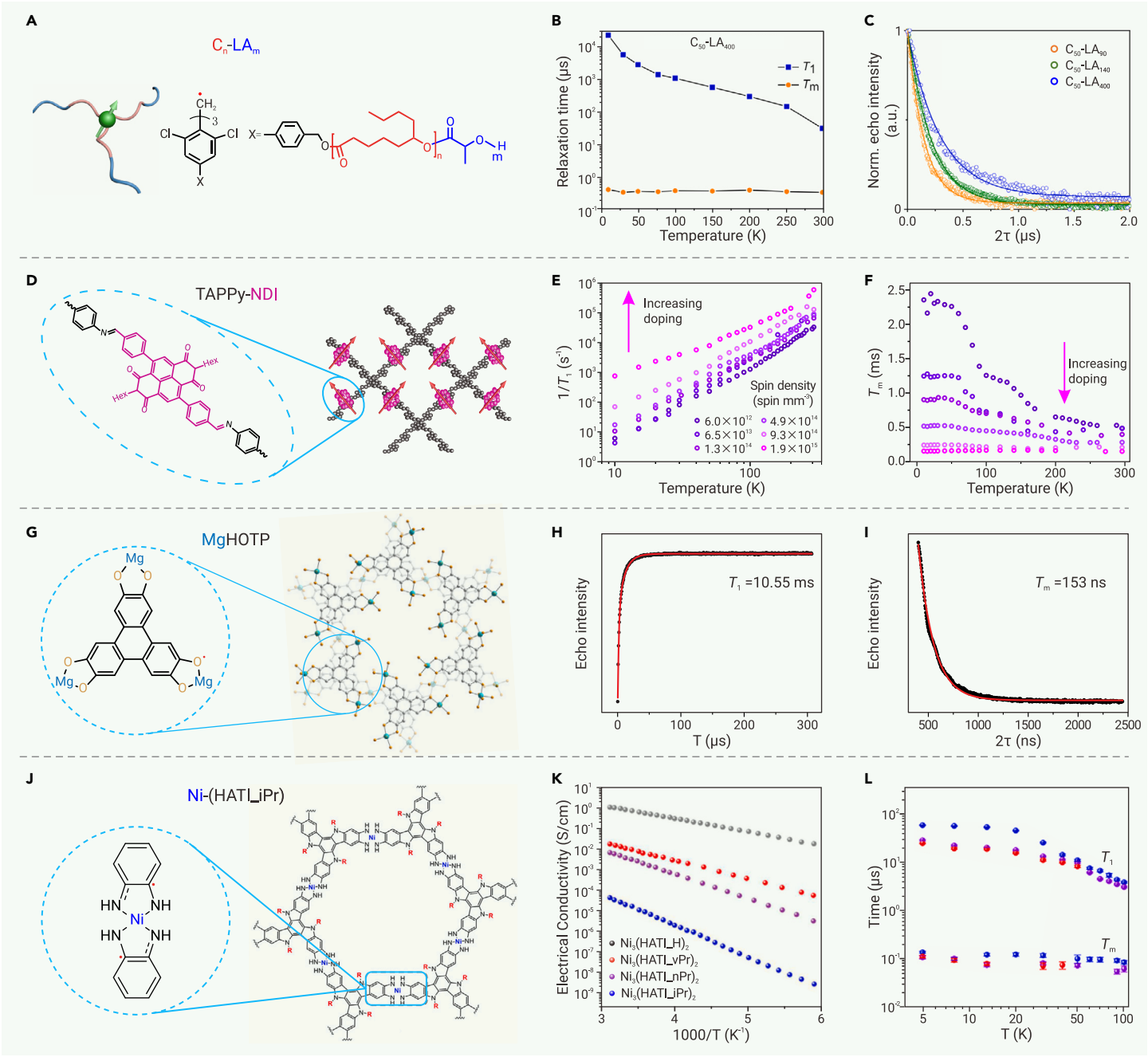

Figure 6. Integration of radical qubits in polymers and microporous materials (A–C) (A) Structures, (B) variable-temperature T_1 and T_m, and (C) Hahn echo decay curves (298 K) of C_n-LA_m block copolymers. Reproduced from Hou et al.[110] with permission from John Wiley & Sons, copyright 2024. (D–F) (D) Structure of TAPPy-NDI, and (E and F) concentration and temperature dependencies of its T_1 and T_m. Reproduced from Oanta et al.[112] with permission from American Chemical Society, copyright 2023. (G–I) (G) Structure, (H) inversion recovery curve (296 K), and (I) Hahn echo decay curve (296 K) of MgHOTP. Reproduced from Sun et al.[111] with permission from American Chemical Society, copyright 2022. (J–L) (J) Structure, (K) variable-temperature electrical conductivity, and (L) variable-temperature T_1 and T_m of Ni_3(HATI_X)$_2$. Reproduced from Lu et al.[113] with permission from American Chemical Society, copyright 2024.

modulate spin-lattice relaxation and decoherence, respectively. Meanwhile, substrates of thin films and SAMs could also affect spin dynamics by providing a vastly different phononic, electrical, and/or magnetic environment.[172–174] Therefore, it is critical to articulate structure-spin dynamics relationships of radical qubits in solid state to optimize their performance in practical applications. We summarize recent advances in solid-state-integrated radical qubits and list their spin dynamic properties in Table S3.

Organic polymers could integrate radicals as monomers. The spatial distribution of radicals could be designed by side-chain engineering or block copolymer self-assembly. Hou et al. integrated chlorine-substituted triphenylmethyl radicals into a series of block copolymers with diblock polyesters (Figure 6A).[110] The processability of these block copolymers allows easy preparation of thin films. Annealing-induced phase separation leads to self-assemblies with various morphologies, including sphere, lamellae, cylinder, and gyroid. These morphologies are determined by the structures and lengths of polyesters. This morphological control allows for the tuning of spin-spin distances, which in turn affects spin dynamics. Both T_1 and T_m increase with the length of the polyesters (Figure 6C). Importantly, some of these films show room temperature coherence, with one example (C_{50}-LA_{400}) exhibiting T_1 = 29.23 μs and T_m = 0.318 μs at 298 K (Figure 6B). Therefore, these thin films of block copolymers behave as tunable qubits.

Different from organic polymers that are mostly amorphous, MOFs and COFs are crystalline microporous materials with designable structures through reticular chemistry. MOFs are composed of inorganic nodes connected by organic linkers through coordination bonds, whereas COFs consist of purely organic monomers with covalent linkages.[175,176] By using stable radicals as building blocks, one can construct ordered arrays of qubits with predefined spin-spin

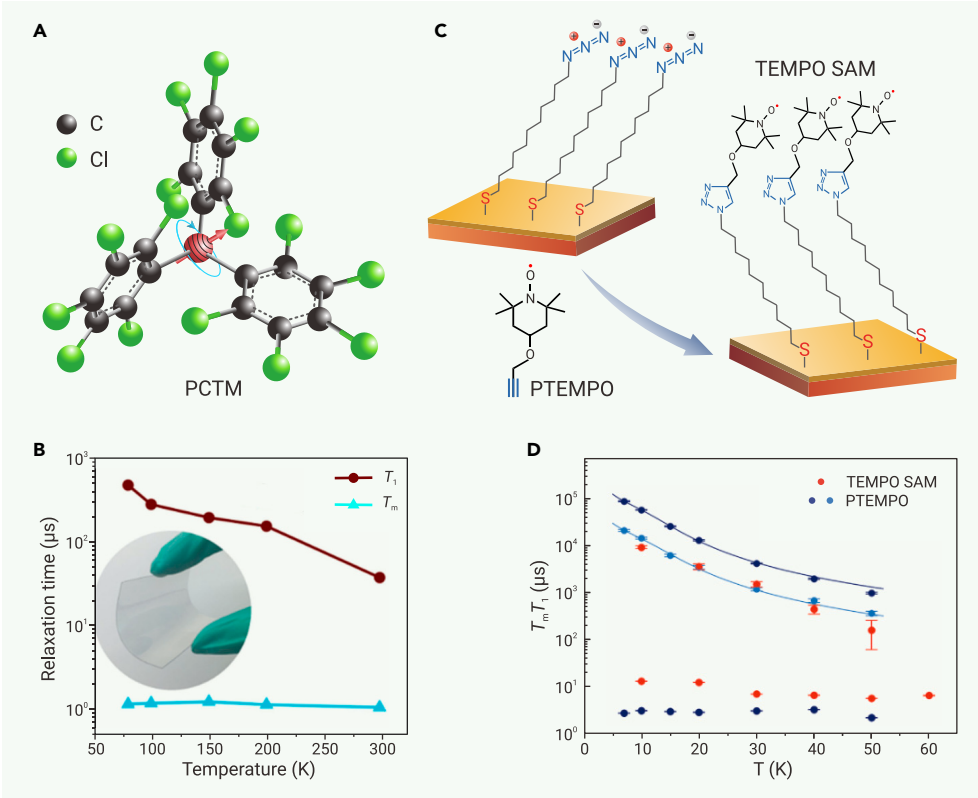

Figure 7. Integration of radical qubits in thin films and SAMs (A and B) (A) Structure and (B) variable-temperature T_1 and T_m of thin films of the PCTM radical. Reproduced from Dai et al.[114] with permission from John Wiley & Sons, copyright 2018. (C) Fabrication of TEMPO SAM on a gold surface. (D) Temperature dependencies of T_1 and T_m for the TEMPO SAM and a dilute solution of TEMPO (PTEMPO). (C and D) Reproduced from Tesi et al.[115] distributed under CC-BY 4.0 (http://creativecommons.org/licenses/by/4.0/).

distances and orientations. The modular lattices enable precise control over frequencies and density of states of phonons.[177,178] Moreover, the microporosity facilitates post-synthetic modification of radical concentration with redox chemistry.[179] These enable fine-tuning of spin-spin interaction and spin-phonon coupling, offering opportunities for systematic investigation of the structure-spin dynamics relationship, which provides guidelines for optimizing the T_1 and T_m of radical qubits in framework materials.

As a proof of concept, Oanta et al. synthesized a layered COF (TAPPy-NDI) containing naphthalene diimide (NDI), which can be post-synthetically reduced by cobaltocene to generate $NDI^{\cdot-}$ radicals (Figure 6D).[112] Controlling the stoichiometry between NDI and cobaltocene gives rise to a wide range of spin concentrations spanning from 6.0×10^{12} to 1.9×10^{15} mm^{-3}. Both T_1 and T_m increase with decreasing spin concentration from 10 to 296 K, indicating that the spin-spin interaction plays a key role in both spin relaxation and decoherence (Figures 6E and 6F). In addition, the spin concentration strongly tweaks the decoherence mechanism. When it is low, the temperature dependence of T_m from 10 to 296 K exhibits various plateaus and declines, indicating that the decoherence is caused by spectral diffusion from nuclear spins, rotary functional groups, and spin relaxation at different temperature regions (Figure 6F). As the spin concentration increases, the temperature dependence of T_m gradually diminishes and eventually disappears, indicating that instantaneous diffusion becomes the dominant factor. Indeed, the spin concentration controls both spin dynamics and electrical conductivity of this COF,[180] rendering it a material that can be fine-tuned by guest molecules and potentially controlled by a gate.

MOFs utilize metal ions as building blocks, resulting in versatile structures and functionalities. However, these metal ions may also introduce additional sources of decoherence due to their electron and nuclear spins. Metal ions should be diamagnetic and should possess few nuclear spins. Choices include Mg^{2+}, Ca^{2+}, Ti^{4+}, Zn^{2+}, Zr^{4+}, octahedrally coordinated low-spin Fe^{2+}, square-planarly coordinated Ni^{2+}, etc. The combination of these metal ions with stable radicals, such as TEMPO and TTF, has led to the synthesis of several MOFs that exhibit electron spin signatures in their continuous wave EPR spectra.[160,162,181] However, studies on their electron spin dynamics are only beginning to emerge. In 2022, Sun et al. reported the spin dynamics of a MOF, MgHOTP, integrating Mg^{2+} and 2,3,6,7,10,11-hexaoxytriphenylene (HOTP), the latter of which is spontaneously oxidized in air to form a semiquinone-like radical (Figure 6G).[111] The powder of this material exhibits T_1 = 10.55 μs (Figure 6H) and T_m = 153 ns at 296 K (Figure 6I), demonstrating the qubit behavior of HOTP-based radicals. Soaking it in tetrahydrofuran (THF) enhances the T_1 to 21.61 μs and the T_m to 202 ns, further demonstrating the guest-tunability of spin dynamics.

Recently, Lu et al. investigated the spin dynamics in a series of layered MOFs, $Ni_3(HATI\_X)_2$, consisting of square-planarly coordinated Ni^{2+} and substituted 2,3,7,8,12,13-hexaiminotriindole (HATI_X) (Figure 6J), where X represents hydrogen (H), allyl (vPr), n-propyl (nPr), or isopropyl (iPr) groups.[113] The substituents interfere with interlayer π-stacking, resulting in an enlarged interlayer distance and dislocated packing. On the one hand, this hampers charge transport and reduces electrical conductivity (Figure 6K); on the other hand, it suppresses phonons and in turn spin-lattice relaxation. Meanwhile, the spin decoherence seems to be governed by the local nuclear and electron spin bath. As a result, $Ni_3(HATI\_iPr)_2$ shows higher T_1 than $Ni_3(HATI\_vPr)_2$ and $Ni_3(HATI\_nPr)_2$ at 5–100 K, yet the T_m values of these three MOFs are almost identical (Figure 6L). Notably, the most conductive analog, $Ni_3(HATI\_H)_2$, does not exhibit electron spin coherence even at 5 K, indicating fast spin relaxation caused by phonon scattering of itinerant electrons through the Elliott-Yafet relaxation mechanism. Thus, this work shows that electron delocalization may deteriorate spin coherence, posing demands on balancing charge transport and spin dynamics in MOFs.

Thin film and surface integration of radical qubits are prerequisites for many device-related applications. The key challenge in fabricating thin films of radical qubits is to suppress decoherence caused by spin-spin interaction. This could be done by diluting the radical with its diamagnetic analog. Dai et al. prepared thin films of a mixture of perchlorinated triphenylmethyl radical (PCTM) and its diamagnetic hydrogenated analog at a molar ratio of 1:1,000 (Figure 7A). These films were deposited onto quartz and polyethylene terephthalate substrates via vapor deposition and spin coating.[114] The PCTM in a film of 200 nm thickness exhibits T_1 = 35.6 μs and T_m = 1.08 μs at 298 K (Figure 7B), which are nearly identical to the values observed for the powder of this molecule, indicating that the substrate does not interfere with spin dynamics in the film. An alternative dilution method is to separate radical qubits by polymers. For instance, dispersing BDPA radicals within polymethyl methacrylate generates thin films exhibiting T_1 = 20–40 ms and $T_m \approx 0.6$ μs at 7 K,[182] and, as discussed above, incorporating chlorine-substituted triphenylmethyl radicals into block copolymers enables further control of film morphology and spatial distribution of radicals. This approach results in tunable quantum coherence at room temperature.[110]

SAM is a useful strategy to integrate functional molecules onto the surface of substrates.[168] Tesi et al. developed a bottom-up method to arrange radical qubits as functional groups of SAMs onto the surface of gold.[115] This method includes two steps: first, an azide-modified alkanethiolate SAM is grown on gold; second, an alkyne-modified TEMPO radical reacts with azide groups via a click reaction, functionalizing the SAM with radical qubits (Figure 7C). A Fabry-Pérot resonator operating at the Q-band frequency was used to characterize spin dynamics of monolayer radicals, revealing T_1 = 9.2 ms and T_m = 13.53 μs at 10 K (Figure 7D). This T_m value exceeds that observed for a dilute solution of TEMPO radicals (PTEMPO) at the same temperature (T_m = 3.23 μs at 10 K) (Figure 7D), verifying that the substrate does not reduce the coherence. The modularity of this method

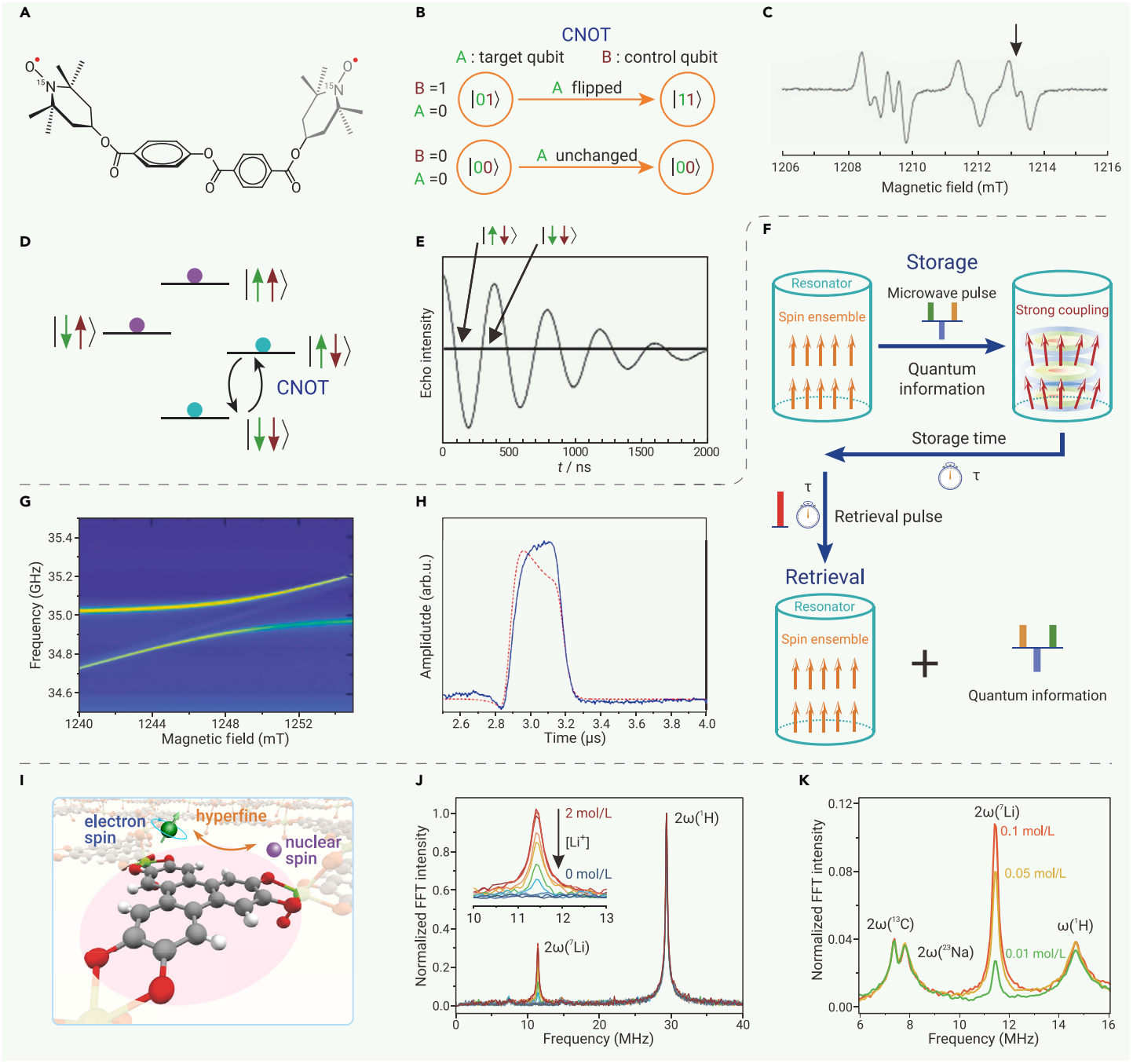

Figure 8. QIS applications of radical qubits (A–E) Molecular quantum logic gate. (A) The molecule containing two ^{15}N- and ^{2}H-substituted TEMPO radicals used for the CNOT gate implementation. (B) Schematic illustration of the CNOT gate. (C) Continuous wave (CW) EPR spectrum of the biradical molecule. The arrow points to the resonance field at which the CNOT gate is implemented. (D) Schematic energy diagram of four zero-field split electron spin states of the biradical molecule. (E) Manifestation of the CNOT gate through the Rabi oscillation. (C–E) reproduced from Nakazawa et al.[48] with permission from John Wiley & Sons, copyright 2021. (F–H) Molecular quantum memory. (F) Conceptual illustration of quantum memory. (G) Avoided crossing in a 2D CW EPR spectrum of BDPA·Bz radicals showing the strong coupling between electron spins and the microwave cavity. (H) A spin echo that shows the retrieval of quantum information stored in the quantum memory for 1.4 μs. Reproduced from Lenz et al.[188] distributed under CC-BY 4.0 (http://creativecommons.org/licenses/by/4.0/). (I–K) Molecular quantum sensing. (I) Conceptual illustration of quantum sensing harnessing hyperfine interaction between MOF-integrated radicals and nuclear spins of adsorbed ions. (J) CP-ESEEM spectra of MgHOTP in THF solutions with various concentrations of Li^+. (K) CP-ESEEM spectra of MgHOTP in THF solutions consisting of both Li^+ and Na^+. Reproduced from Sun et al.[111] with permission from American Chemical Society, copyright 2022.

points out opportunities for further functionalization of the SAM, which might open the door for SAM-based QIS applications.

APPLICATIONS IN QUANTUM INFORMATION SCIENCE

In this section, we summarize proof-of-concept QIS applications of radical qubits reported so far, including quantum computing, quantum memory, and quantum sensing.

Quantum computing runs quantum algorithms capable of solving problems that are practically unsolvable for classical computers, such as factoring large numbers.[183,184] The implementation of quantum algorithms can be decomposed into a set of single-qubit and two-qubit universal quantum logic gates.[185] The latter, e.g., CNOT and iSWAP gates, require quantum entanglement between qubits, which could be established by qubit-qubit interaction.[186,187] To this end, two radical qubits can be integrated into a single molecule with a designated spin-spin interaction by sophisticated molecular design. Their weak spin-orbit coupling and hyperfine coupling give rise to narrow resonant linewidths that facilitate implementation of two-qubit quantum logic gates. Nakazawa et al. designed a molecule containing two TEMPO radicals separated by 2 nm (Figure 8A) and realized the CNOT gate with this molecule.[48] The TEMPO moieties are enriched with the isotopes by ^{15}N and ^{2}H to simplify the hyperfine structures and narrow

the EPR spectrum linewidths. The z axes of *g*-tensors of the two radicals and the spin dipolar tensor are not co-linear due to the non-linear molecular structure. These features enable implementation of the CNOT gate with this two-qubit molecule (Figure 8B). With a specific orientation of a single crystal mounted in a Q-band pulse EPR spectrometer, the transition frequencies of $|\downarrow\downarrow\rangle \Rightarrow |\uparrow\downarrow\rangle$ and $|\downarrow\uparrow\rangle \Rightarrow |\uparrow\uparrow\rangle$ differ by 9.5 MHz, which exceeds their linewidths (Figure 8C). Thus, when the magnetic field is tuned resonant with the first transition, the first spin can be flipped only when the second spin is in the $|\downarrow\rangle$ state (Figure 8D). With the second spin as the control qubit and the first spin as the target qubit, a π pulse of 200 ns achieves the CNOT gate operation (Figures 8B and 8E). Although a rigorous benchmarking of the CNOT gate remains to be conducted, this demonstration shows the potential of tailor-design multi-qubit molecules for implementing quantum logic gates, which is a cornerstone for molecular quantum computing.

Quantum memories allow for the storage and retrieval of quantum information (Figure 8F), which is essential for quantum computing and long-distance quantum communication.[189–194] Lenz et al. fabricated a quantum memory with an ensemble of a stable organic radical (benzene complex of BDPA, BDPA·Bz) coupled with a three-dimensional Fabry-Pérot microwave resonator.[188] The large number of spins (6×10^{18} spins) dramatically improves the spin-photon coupling strength that surpasses both the spin decoherence rate and the cavity dissipation rate, establishing strong coupling between the spin ensemble and the cavity (Figure 8G). Such strong coupling improves the T_m of the radical even at room temperature thanks to the cavity protection effect and enables spin-photon entanglement. At 7 K, a weak microwave pulse can transfer the quantum information conveyed by the microwave photons to the spin ensemble. This quantum information can be stored for 1.4 μs and then retrieved to microwave photons by a strong microwave pulse (Figure 8H). Thus, these results demonstrate that the spin-ensemble-resonator hybrid system can be used as a quantum memory.

Quantum sensing harnesses a quantum system, a quantum property, or a quantum phenomenon to measure a physical quantity, such as magnetic field, temperature, and frequency.[143] Radical qubits can be used to detect nuclear spins at relatively high temperature via quantum sensing: when a nuclear spin is weakly coupled to the electron spin, it not only causes spin relaxation and decoherence of the radical but also modulates its Larmor precession. The modulation frequency is related to the Larmor frequency of the nuclear spin and the modulation intensity scales with the number of nuclear spins surrounding the radical, enabling both identification and quantification of the nuclear spin. Driven by this idea, Sun et al. designed a MOF, MgHOTP, containing semiquinone-like radicals (Figure 6G) and demonstrated quantum sensing of Li^+ at room temperature in THF solution.[111] The microporosity of this material allows diffusion of Li^+ into the nanometer-size pores, enforcing close contact and weak hyperfine interaction between radicals and Li^+ (Figure 8I). Relaxometry shows decreasing T_1 and T_m with increasing concentration of Li^+ in the range of 0.5–2 mol/L. Hyperfine spectroscopy (combination-peak electron spin echo envelope modulation, CP-ESEEM) reveals a modulation frequency corresponding to the Larmor frequency of Li^+. The modulation intensity increases with the concentration of Li^+ in the range of 5×10^{-3} to 0.5 mol/L (Figure 8J). Furthermore, because many nuclear spins exhibit unique Larmor frequencies, the hyperfine spectroscopy can detect multiple nuclear spins simultaneously and unambiguously, exemplified by Li^+ and Na^+ in this work (Figure 8K). Thus, radical qubits hold the promise for chemical-specific quantum sensing in complex environments and at room temperature.

Beyond nuclear spins, radical qubits could also be used for quantum sensing of magnetic field. Bonizzoni et al. integrated BDPA radicals into a coplanar microwave resonator, developed quantum sensing protocols based on dynamical decoupling pulse sequences, and performed echo detection to sense alternative-current magnetic field with a sensitivity reaching 10^{-9} T/Hz$^{1/2}$.[195] In addition, radical-based quantum superposition and quantum sensing have been hypothesized to be essential for bird navigation.[196] For example, it is proposed that the illumination of cryptochromes in birds' eyes produces $FAD^{\cdot -}$ (FAD, flavin adenine dinucleotide) radical pairs with strong and anisotropic hyperfine coupling with ^{14}N. Acting as magnetic orientation sensors, these radical pairs might allow birds to detect the Earth's magnetic field and keep them oriented during migration.[197–199]

SUMMARY AND OUTLOOKS

In this review, we summarize spin dynamic properties, mechanisms, and their optimization strategies of stable organic radicals, present their integration into solid-state materials and surface structures, and enumerate their prototypical applications in quantum computing, quantum memory, and quantum sensing. Besides the room temperature quantum coherence and versatile integrability that have been discussed extensively above, radical qubits distinguish from other types of qubits by their atomic-level rational designability. Their bottom-up synthesis allows for precise control over the structural rigidity as well as the type, amount, and spatial distribution of nuclear spins and functional groups surrounding the electron spin. This precise control is crucial for prolonging both the T_1 and T_m. Such synthetic versatility also facilitates rational design of radical qubits for QIS: multiple radical qubits could be incorporated into one molecule with prescribed inter-qubit interactions to implement specific quantum logic gates, luminescent radical qubits may introduce spin-optical interfaces that are essential for quantum communication,[58,200] and radical qubits functionalized by molecular/ionic recognition groups may enable highly selective quantum sensing, and their integration with photo-excited triplets may lead to complex molecular qubit systems with versatile functionalities.[201,202] Thanks to these unique advantages, stable organic radical qubits could promote the development of quantum information technologies that demand compatibility with room temperature and complex chemical environments. This would facilitate QIS applications in biological systems, energy storage devices, electronics, environmental monitoring, and more.

With their great potential in QIS applications, stable organic radical qubits pose many opportunities and challenges for future research. First, besides the radical qubits listed in Tables 1 and S2, many others remain to be characterized from the QIS perspective, such as 7,7,8,8-tetracyanoquinonedimethane mono-anion radical, perylene cation radical, dithiophenalenyl radical and their derivatives, among others. Second, spin dynamics of radical qubits need to be investigated in various application-related scenarios. Integration of radical qubits into microporous materials, thin films, and devices necessitates in-depth examination of spin relaxation and decoherence mechanisms because these structures introduce complex phononic, magnetic, and electrical environments. Third, to take full advantage of radical qubits for QIS, strategies need to be developed to achieve high-fidelity initialization, manipulation, and readout of single radical qubits in mild conditions. This is technically difficult because thermal initialization requires a strong magnetic field and ultralow temperature, while conventional EPR-based spin state readout only works for ensembles.[202] To this end, we could learn from the addressing strategies of other types of qubits. Optical pumping and spin injection may be implemented to initialize radicals.[15,203,204] Optical,[35–37] electrical,[44,45,205] scanning probe microscopic,[46] and quantum metrological strategies[47,206] could be sufficiently sensitive to detect single electron spins. In addition, recent studies of the chirality-induced spin selectivity effect may offer an ultimate solution to initialize and readout single electron spins with chiral moieties embedded in radicals.[207] Finally, efforts should be paid to improve scalability of radical qubits, which requires coherent addressing of each qubit in a system. This is challenging for conventional EPR as most radicals exhibit similar *g*-factors (close to 2.0023) and can hardly be spectrally distinguished. Implementing radical qubits into single-molecule spintronic devices may enable spatial addressing of individual qubits, leading to fabrication of universal molecular quantum computers.

REFERENCES

1. Heinrich, A.J., Oliver, W.D., Vandersypen, L.M.K., et al. (2021). Quantum-coherent nanoscience. Nat. Nanotechnol. ***16***: 1318–1329. https://doi.org/10.1038/s41565-021-00994-1.
2. Pelucchi, E., Fagas, G., Aharonovich, I., et al. (2021). The potential and global outlook of integrated photonics for quantum technologies. Nat. Rev. Phys. ***4***: 194–208.
3. MacQuarrie, E.R., Simon, C., Simmons, S., et al. (2020). The emerging commercial landscape of quantum computing. Nat. Rev. Phys. ***2***: 596–598. https://doi.org/10.1038/s42254-020-00247-5.
4. Joseph, D., Misoczki, R., Manzano, M., et al. (2022). Transitioning organizations to post-quantum cryptography. Nature ***605***: 237–243. https://doi.org/10.1038/s41586-022-04623-2.

5. Arute, F., Arya, K., Babbush, R., et al. (2019). Quantum supremacy using a programmable superconducting processor. Nature ***574***: 505–510. https://doi.org/10.1038/s41586-019-1666-5.
6. Zhong, H.-S., Wang, H., Deng, Y.-H., et al. (2020). Quantum computational advantage using photons. Science ***370***: 1460–1463. https://doi.org/10.1126/science.abe8770.
7. Yin, J., Cao, Y., Li, Y.-H., et al. (2017). Satellite-based entanglement distribution over 1200 kilometers. Science ***356***: 1140–1144. https://doi.org/10.1126/science.aan3211.
8. Liao, S.-K., Cai, W.-Q., Liu, W.-Y., et al. (2017). Satellite-to-ground quantum key distribution. Nature ***549***: 43–47. https://doi.org/10.1038/nature23655.
9. Le Sage, D., Arai, K., Glenn, D.R., et al. (2013). Optical magnetic imaging of living cells. Nature ***496***: 486–489. https://doi.org/10.1038/nature12072.
10. Aslam, N., Zhou, H., Urbach, E.K., et al. (2023). Quantum sensors for biomedical applications. Nat. Rev. Phys. ***5***: 157–169. https://doi.org/10.1038/s42254-023-00558-3.
11. DiVincenzo, D.P. (2000). The physical implementation of quantum computation. Fortschr. Phys. ***48***: 771–783. https://doi.org/10.1002/1521-3978(200009)48:9/11<771::AID-PROP771>3.0.CO;2-E.
12. Blais, A., Grimsmo, A.L., Girvin, S.M., et al. (2021). Circuit quantum electrodynamics. Rev. Mod. Phys. ***93***: 025005. https://doi.org/10.1038/nphys1730.
13. Kloeffel, C., and Loss, D. (2013). Prospects for spin-based quantum computing in quantum dots. Annu. Rev. Condens. Matter Phys. ***4***: 51–81. https://doi.org/10.1146/annurev-conmatphys-030212-184248.
14. Bruzewicz, C.D., Chiaverini, J., McConnell, R., et al. (2019). Trapped-ion quantum computing: progress and challenges. Appl. Phys. Rev. ***6***: 021314. https://doi.org/10.1063/1.5088164.
15. Saffman, M. (2016). Quantum computing with atomic qubits and Rydberg interactions: progress and challenges. J. Phys. B Atom. Mol. Opt. Phys. ***49***: 202001. https://doi.org/10.1088/0953-4075/49/20/202001.
16. Pla, J.J., Tan, K.Y., Dehollain, J.P., et al. (2013). High-fidelity readout and control of a nuclear spin qubit in silicon. Nature ***496***: 334–338. https://doi.org/10.1038/nature12011.
17. Vandersypen, L.M.K., and Chuang, I.L. (2005). NMR techniques for quantum control and computation. Rev. Mod. Phys. ***76***: 1037–1069. https://doi.org/10.1103/RevModPhys.76.1037.
18. Zhou, J.-W., Wang, P.-F., Shi, F.-Z., et al. (2014). Quantum information processing and metrology with color centers in diamonds. Front. Physiol. ***9***: 587–597. https://doi.org/10.1007/s11467-014-0421-5.
19. Doherty, M.W., Manson, N.B., Delaney, P., et al. (2013). The nitrogen-vacancy colour centre in diamond. Phys. Rep. ***528***: 1–45. https://doi.org/10.1016/j.physrep.2013.02.001.
20. Bourgeois, E., Gulka, M., and Nesladek, M. (2020). Photoelectric detection and quantum readout of nitrogen-vacancy center spin states in diamond. Adv. Opt. Mater. ***8***: 1902132. https://doi.org/10.1002/adom.201902132.
21. Sarma, S.D., Freedman, M., and Nayak, C. (2015). Majorana zero modes and topological quantum computation. Inform ***1***: 15001. https://doi.org/10.1038/npjqi.2015.1.
22. Popkin, G. (2016). Quest for qubits. Science ***354***: 1090–1093. https://doi.org/10.1126/science.354.6316.1090.
23. Wasielewski, M.R., Forbes, M.D.E., Frank, N.L., et al. (2020). Exploiting chemistry and molecular systems for quantum information science. Nat. Rev. Chem ***4***: 490–504. https://doi.org/10.1038/s41570-020-0200-5.
24. Atzori, M., and Sessoli, R. (2019). The second quantum revolution: role and challenges of molecular chemistry. J. Am. Chem. Soc. ***141***: 11339–11352. https://doi.org/10.1021/jacs.9b00984.
25. Yu, C.-J., von Kugelgen, S., Laorenza, D.W., et al. (2021). A molecular approach to quantum sensing. ACS Cent. Sci. ***7***: 712–723. https://doi.org/10.1021/acscentsci.0c00737.
26. Mani, T. (2022). Molecular qubits based on photogenerated spin-correlated radical pairs for quantum sensing. Chem. Phys. Rev. ***3***: 021301. https://doi.org/10.1063/5.0084072.
27. Graham, M.J., Zadrozny, J.M., Fataftah, M.S., et al. (2017). Forging solid-state qubit design principles in a molecular furnace. Chem. Mater. ***29***: 1885–1897. https://doi.org/10.1021/acs.chemmater.6b05433.
28. Kukkar, D., Vellingiri, K., Kim, K.-H., et al. (2018). Recent progress in biological and chemical sensing by luminescent metal-organic frameworks. Sensor. Actuator. B Chem. ***273***: 1346–1370. https://doi.org/10.1016/j.snb.2018.06.128.
29. Rasouli, Z., and Ghavami, R. (2020). Facile approach to fabricate a chemical sensor array based on nanocurcumin–metal ions aggregates: detection and identification of DNA nucleobases. ACS Omega ***5***: 19331–19341. https://doi.org/10.1021/acsomega.0c00593.
30. Ullah, F., Khan, T.A., Iltaf, J., et al. (2022). Heterocyclic crown ethers with potential biological and pharmacological properties: from synthesis to applications. Appl. Sci. ***12***: 1102. https://doi.org/10.3390/app12031102.
31. Fu, P.-X., Zhou, S., Liu, Z., et al. (2022). Multiprocessing quantum computing through hyperfine couplings in endohedral fullerene derivatives. Angew. Chem. Int. Ed. ***61***: e202212939. https://doi.org/10.1002/anie.202212939.
32. Zadrozny, J.M., Niklas, J., Poluektov, O.G., et al. (2015). Millisecond coherence time in a tunable molecular electronic spin qubit. ACS Cent. Sci. ***1***: 488–492. https://doi.org/10.1021/acscentsci.5b00338.
33. Atzori, M., Tesi, L., Morra, E., et al. (2016). Room-temperature quantum coherence and Rabi oscillations in vanadyl phthalocyanine: toward multifunctional molecular spin qubits. J. Am. Chem. Soc. ***138***: 2154–2157. https://doi.org/10.1021/jacs.5b13408.
34. Fataftah, M.S., Krzyaniak, M.D., Vlaisavljevich, B., et al. (2019). Metal–ligand covalency enables room temperature molecular qubit candidates. Chem. Sci. ***10***: 6707–6714. https://doi.org/10.1039/C9SC00074G.
35. Wrachtrup, J., von Borczyskowski, C., Bernard, J., et al. (1993). Optical detection of magnetic resonance in a single molecule. Nature ***363***: 244–245. https://doi.org/10.1038/363244a0.
36. Wrachtrup, J., von Borczyskowski, C., Bernard, J., et al. (1993). Optically detected spin coherence of single molecules. Phys. Rev. Lett. ***71***: 3565–3568. https://doi.org/10.1103/PhysRevLett.71.3565.
37. Köhler, J., Disselhorst, J.A.J.M., Donckers, M.C.J.M., et al. (1993). Magnetic resonance of a single molecular spin. Nature ***363***: 242–244. https://doi.org/10.1038/363242a0.
38. Bayliss, S.L., Laorenza, D.W., Mintun, P.J., et al. (2020). Optically addressable molecular spins for quantum information processing. Science ***370***: 1309–1312. https://doi.org/10.1126/science.abb9352.
39. Singh, H., D'Souza, N., Zhong, K., et al. (2024). Room-temperature quantum sensing with photoexcited triplet electrons in organic crystals. Preprint at arXiv. https://doi.org/10.48550/arXiv.2402.13898.
40. Mena, A., Mann, S.K., Cowley-Semple, A., et al. (2024). Room-temperature Optically Detected Coherent Control of Molecular Spins. Preprint at arXiv. https://doi.org/10.1038/s41563-024-01803-5.
41. Ariciu, A.-M., Woen, D.H., Huh, D.N., et al. (2019). Engineering electronic structure to prolong relaxation times in molecular qubits by minimising orbital angular momentum. Nat. Commun. ***10***: 3330. https://doi.org/10.1038/s41467-019-11309-3.
42. Laorenza, D.W., Kairalapova, A., Bayliss, S.L., et al. (2021). Tunable Cr^{4+} molecular color centers. J. Am. Chem. Soc. ***143***: 21350–21363. https://doi.org/10.1021/jacs.1c10145.
43. Fataftah, M.S., Bayliss, S.L., Laorenza, D.W., et al. (2020). Trigonal bipyramidal V^{3+} complex as an optically addressable molecular qubit candidate. J. Am. Chem. Soc. ***142***: 20400–20408. https://doi.org/10.1021/jacs.0c08986.
44. Zhang, X., Wolf, C., Wang, Y., et al. (2022). Electron spin resonance of single iron phthalocyanine molecules and role of their non-localized spins in magnetic interactions. Nat. Chem. ***14***: 59–65. https://doi.org/10.1038/s41557-021-00827-7.
45. Willke, P., Bilgeri, T., Zhang, X., et al. (2021). Coherent spin control of single molecules on a surface. ACS Nano ***15***: 17959–17965. https://doi.org/10.1021/acsnano.1c06394.
46. Sellies, L., Spachtholz, R., Bleher, S., et al. (2023). Single-molecule electron spin resonance by means of atomic force microscopy. Nature ***624***: 64–68. https://doi.org/10.1038/s41586-023-06754-6.
47. Shi, F., Zhang, Q., Wang, P., et al. (2015). Protein imaging. Single-protein spin resonance spectroscopy under ambient conditions. Science ***347***: 1135–1138. https://doi.org/10.1126/science.aaa225.
48. Nakazawa, S., Nishida, S., Ise, T., et al. (2012). A synthetic two-spin quantum bit: g-engineered exchange-coupled biradical designed for controlled-not gate operations. Angew. Chem. Int. Ed. ***51***: 9860–9864. https://doi.org/10.1002/anie.201204489.
49. Mao, H., Pažéra, G.J., Young, R.M., et al. (2023). Quantum gate operations on a spectrally addressable photogenerated molecular electron spin-qubit pair. J. Am. Chem. Soc. ***145***: 6585–6593. https://doi.org/10.1021/jacs.3c01243.
50. Jee, B., Hartmann, M., and Pöppl, A. (2013). H_2, D_2 and HD adsorption upon the metal-organic framework $[Cu_{2.97}Zn_{0.03}(btc)_2]_n$ studied by pulsed ENDOR and HYSCORE spectroscopy. Mol. Phys. ***111***: 2950–2966. https://doi.org/10.1080/00268976.2013.795666.
51. Rugg, B.K., Krzyaniak, M.D., Phelan, B.T., et al. (2019). Photodriven quantum teleportation of an electron spin state in a covalent donor–acceptor–radical system. Nat. Chem. ***11***: 981–986. https://doi.org/10.1038/s41557-019-0332-8.
52. Aguilà, D., Roubeau, O., and Aromí, G. (2021). Designed polynuclear lanthanide complexes for quantum information processing. Dalton Trans. ***50***: 12045–12057. https://doi.org/10.1039/D1DT01862K.
53. Harvey, S.M., and Wasielewski, M.R. (2021). Photogenerated spin-correlated radical pairs: from photosynthetic energy transduction to quantum information science. J. Am. Chem. Soc. ***143***: 15508–15529. https://doi.org/10.1021/jacs.1c07706.
54. Eaton, S.S., and Eaton, G.R. (2018). Relaxation mechanisms. In EPR Spectroscopy: Fundamentals and Methods, D. Goldfarb and S. Stoll, eds. (Wiley), pp. 175–192.
55. Abe, M. (2013). Diradicals. Chem. Rev. ***113***: 7011–7088. https://doi.org/10.1021/cr400056a.
56. Chen, Z.X., Li, Y., and Huang, F. (2021). Persistent and stable organic radicals: design, synthesis, and applications. Chem ***7***: 288–332. https://doi.org/10.1016/j.chempr.2020.09.024.
57. Hicks, R.G. (2010). Stable Radicals: Fundamentals and Applied Aspects of Odd-Electron Compounds (Wiley).
58. Gorgon, S., Lv, K., Grüne, J., et al. (2023). Reversible spin-optical interface in luminescent organic radicals. Nature ***620***: 538–544. https://doi.org/10.1038/s41586-023-06222-1.
59. Mizuno, A., Matsuoka, R., Mibu, T., et al. (2024). Luminescent radicals. Chem. Rev. ***124***: 1034–1121. https://doi.org/10.1021/acs.chemrev.3c00613.
60. Yuan, Y., Yang, J., and Lei, A. (2021). Recent advances in electrochemical oxidative cross-coupling with hydrogen evolution involving radicals. Chem. Soc. Rev. ***50***: 10058–10086. https://doi.org/10.1039/D1CS00150G.
61. Sun, X., Yan, X., Song, K., et al. (2023). A pyrazine-based 2D conductive metal-organic framework for efficient lithium storage. Chin. J. Chem. ***41***: 1691–1696. https://doi.org/10.1002/cjoc.202200819.
62. Kumar, S., Kumar, Y., Keshri, S., et al. (2016). Recent advances in organic radicals and their magnetism. Magnetochemistry ***2***: 42. https://doi.org/10.3390/magnetochemistry2040042.
63. Ribas, X., Maspoch, D., Wurst, K., et al. (2006). Coordination capabilities of a novel organic polychlorotriphenylmethyl monosulfonate radical. Inorg. Chem. ***45***: 5383–5392. https://doi.org/10.1021/ic060182j.

64. Kimura, S., Uejima, M., Ota, W., et al. (2021). An open-shell, luminescent, two-dimensional coordination polymer with a honeycomb lattice and triangular organic radical. J. Am. Chem. Soc. ***143***: 4329–4338. https://doi.org/10.1021/jacs.0c13310.
65. Poderi, C., Neira, I., Franchi, P., et al. (2023). EPR sensing of a cation species by aza-crown ethers incorporating a persistent nitroxidic radical unit. Chem. Eur J. ***29***: e202301508. https://doi.org/10.1002/chem.202301508.
66. Parsaee, F., Senarathna, M.C., Kannangara, P.B., et al. (2021). Radical philicity and its role in selective organic transformations. Nat. Rev. Chem ***5***: 486–499. https://doi.org/10.1038/s41570-021-00284-3.
67. Düz, A.B., Önen, A., and Yağcı, Y. (1998). Photoinduced synthesis and reactions of stable-radical-incorporated poly(methyl methacrylate). Angew. Makromol. Chem. ***258***: 1–4. https://doi.org/10.1002/(SICI)1522-9505(19980801)258:1<1::AID-APMC1>3.0.CO;2-2.
68. Li, P., Xie, T., Duan, X., et al. (2010). A new highly selective and sensitive assay for fluorescence imaging of ·OH in living cells: effectively avoiding the interference of peroxynitrite. Chem. Eur J. ***16***: 1834–1840. https://doi.org/10.1002/chem.200901514.
69. Ji, L., Shi, J., Wei, J., et al. (2020). Air-stable organic radicals: new-generation materials for flexible electronics? Adv. Mater. ***32***: e1908015. https://doi.org/10.1002/adma.201908015.
70. Tan, Y., Hsu, S.-N., Tahir, H., et al. (2022). Electronic and spintronic open-shell macromolecules, Quo Vadis? J. Am. Chem. Soc. ***144***: 626–647. https://doi.org/10.1021/jacs.1c09815.
71. Cui, X., Zhang, Z., Yang, Y., et al. (2022). Organic radical materials in biomedical applications: state of the art and perspectives. Exploration ***2***: 20210264. https://doi.org/10.1002/EXP.20210264.
72. Datta, S.N., Pal, A.K., and Panda, A. (2023). Design of magnetic organic molecules and organic magnets: experiment, theory and computation with application and recent advances. Chem. Phys. Impact ***7***: 100379. https://doi.org/10.1016/j.chphi.2023.100379.
73. Huang, B., Mao, L., Shi, X., et al. (2021). Recent advances and perspectives on supramolecular radical cages. Chem. Sci. ***12***: 13648–13663. https://doi.org/10.1039/D1SC01618K.
74. Dasgupta, A., Richards, E., and Melen, R.L. (2021). Frustrated radical pairs: insights from EPR spectroscopy. Angew. Chem. Int. Ed. ***60***: 53–65. https://doi.org/10.1021/acs.chemrev.3c00406.
75. Shu, C., Yang, Z., and Rajca, A. (2023). From stable radicals to thermally robust high-spin diradicals and triradicals. Chem. Rev. ***123***: 11954–12003. https://doi.org/10.1021/acs.chemrev.3c00406.
76. Torricella, F., Pierro, A., Mileo, E., et al. (2021). Nitroxide spin labels and EPR spectroscopy: a powerful association for protein dynamics studies. Biochim. Biophys. Acta, Proteins Proteomics ***1869***: 140653. https://doi.org/10.1016/j.bbapap.2021.140653.
77. Gauto, D., Dakhlaoui, O., Marin-Montesinos, I., et al. (2021). Targeted DNP for biomolecular solid-state NMR. Chem. Sci. ***12***: 6223–6237. https://doi.org/10.1039/D0SC06959K.
78. Harneit, W. (2017). Spin quantum computing with endohedral fullerenes. In Endohedral Fullerenes: Electron Transfer and Spin, A.A. Popov, ed. (Springer), pp. 297–324.
79. Zhou, S., Yuan, J., Wang, Z., et al. (2022). Implementation of quantum level addressability and geometric phase manipulation in aligned endohedral fullerene qudits. Angew. Chem. Int. Ed. ***61***: e202115263. https://doi.org/10.1002/anie.202115263.
80. Brown, R.M., Ito, Y., Warner, J.H., et al. (2010). Electron spin coherence in metallofullerenes: Y, Sc, and La@C_{82}. Phys. Rev. B ***82***: 033410. https://doi.org/10.1103/PhysRevB.82.033410.
81. Mayländer, M., Kopp, K., Nolden, O., et al. (2023). PDI–trityl dyads as photogenerated molecular spin qubit candidates. Chem. Sci. ***14***: 10727–10735. https://doi.org/10.1039/D3SC04375D.
82. Mayländer, M., Thielert, P., Quintes, T., et al. (2023). Room temperature electron spin coherence in photogenerated molecular spin qubit candidates. J. Am. Chem. Soc. ***145***: 14064–14069. https://doi.org/10.1021/jacs.3c04021.
83. Quintes, T., Mayländer, M., and Richert, S. (2023). Properties and applications of photoexcited chromophore–radical systems. Nat. Rev. Chem. ***7***: 75–90. https://doi.org/10.1038/s41570-022-00453-y.
84. Schott, S., Chopra, U., Lemaur, V., et al. (2019). Polaron spin dynamics in high-mobility polymeric semiconductors. Nat. Phys. ***15***: 814–822. https://doi.org/10.1038/s41567-019-0538-0.
85. McCamey, D.R., Seipel, H.A., Paik, S.-Y., et al. (2008). Spin Rabi flopping in the photocurrent of a polymer light-emitting diode. Nat. Mater. ***7***: 723–728. https://doi.org/10.1038/nmat2252.
86. Tormyshev, V.M., and Bagryanskaya, E.G. (2021). Trityl radicals: synthesis, properties, and applications. Russ. Chem. Bull. ***70***: 2278–2297. https://doi.org/10.1007/s11172-021-3345-6.
87. Haugland, M.M., Lovett, J.E., and Anderson, E.A. (2017). Advances in the synthesis of nitroxide radicals for use in biomolecule spin labelling. Chem. Soc. Rev. ***47***: 668–680. https://doi.org/10.1039/C6CS00550K.
88. Atsumi, H., Maekawa, K., Nakazawa, S., et al. (2012). Tandem arrays of TEMPO and nitronyl nitroxide radicals with designed arrangements on DNA. Chem. Eur J. ***18***: 178–183. https://doi.org/10.1002/chem.201102693.
89. Jeon, I.-R., Negru, B., VanDuyne, R.P., et al. (2015). A 2D semiquinone radical-containing microporous magnet with solvent-induced switching from T_c = 26 to 80 K. J. Am. Chem. Soc. ***137***: 15699–15702. https://doi.org/10.1021/jacs.5b10382.
90. Mitchell, D.G., Quine, R.W., Tseitlin, M., et al. (2011). Electron spin relaxation and heterogeneity of the 1:1 α,γ-bisdiphenylene-β-phenylallyl (BDPA)/benzene complex. J. Phys. Chem. B ***115***: 7986–7990.
91. Mercier, N., Giffard, M., Pilet, G., et al. (2001). $(TTF)_2$ [TTF $(CO_2H)_2$ $(CO_2)_2$]: a wholly TTF material containing TTF radical cations and TTF derived anions. Chem. Commun. 2722–2723. https://doi.org/10.1039/B108888B.
92. Slota, M., Keerthi, A., Myers, W.K., et al. (2018). Magnetic edge states and coherent manipulation of graphene nanoribbons. Nature ***557***: 691–695. https://doi.org/10.1038/s41586-018-0154-7.
93. Lombardi, F., Lodi, A., Ma, J., et al. (2019). Quantum units from the topological engineering of molecular graphenoids. Science ***366***: 1107–1110. https://doi.org/10.1126/science.aay7203.
94. Chen, Q., Lodi, A., Zhang, H., et al. (2024). Porphyrin-fused graphene nanoribbons. Nat. Chem. https://doi.org/10.1038/s41557-024-01477-1.
95. Chen, J.-S., Trerayapiwat, K.J., Sun, L., et al. (2023). Long-lived electronic spin qubits in single-walled carbon nanotubes. Nat. Commun. ***14***: 848. https://doi.org/10.1038/s41467-023-36031-z.
96. Eaton, S.S., and Eaton, G.R. (2000). Relaxation times of organic radicals and transition metal ions. In Distance Measurements in Biological Systems by EPR, L.J. Berliner, G.R. Eaton, and S.S. Eaton, eds. (Kluwer Academic/Plenum Publishers), pp. 29–154.
97. Wu, M.W., Jiang, J.H., and Weng, M.Q. (2010). Spin dynamics in semiconductors. Phys. Rep. ***493***: 61–236. https://doi.org/10.1016/j.physrep.2010.04.002.
98. Ghim, B.T., Du, J.-L., Pfenninger, S., et al. (1996). Multifrequency electron paramagnetic resonance of irradiated L-alanine. Appl. Radiat. Isot. ***47***: 1235–1239. https://doi.org/10.1016/s0969-8043(96)00037-1.
99. Amdur, M.J., Mullin, K.R., Waters, M.J., et al. (2022). Chemical control of spin–lattice relaxation to discover a room temperature molecular qubit. Chem. Sci. ***13***: 7034–7045. https://doi.org/10.1039/d1sc06130e.
100. Chen, Q., Martin, I., Jiang, L., et al. (2022). Electron spin coherence on a solid neon surface. Quantum Sci. Technol. ***7***: 045016. https://doi.org/10.1038/s41586-022-04539-x.
101. Chen, H., Maryasov, A.G., Rogozhnikova, O.Y., et al. (2016). Electron spin dynamics and spin–lattice relaxation of trityl radicals in frozen solutions. Phys. Chem. Chem. Phys. ***18***: 24954–24965. https://doi.org/10.1039/c6cp02649d.
102. Kuzhelev, A.A., Trukhin, D.V., Krumkacheva, O.A., et al. (2015). Room-temperature electron spin relaxation of triarylmethyl radicals at the X- and Q- bands. J. Phys. Chem. B ***119***: 13630–13640. https://doi.org/10.1021/acs.jpcb.5b03027.
103. Meyer, V., Eaton, S.S., and Eaton, G.R. (2014). X-band electron spin relaxation times for four aromatic radicals in fluid solution and comparison with other organic radicals. Appl. Magn. Reson. ***45***: 993–1007. https://doi.org/10.1007/s00723-014-0579-6.
104. Elajaili, H.B., Biller, J.R., Eaton, S.S., et al. (2014). Frequency dependence of electron spin–lattice relaxation for semiquinones in alcohol solutions. J. Magn. Reson. ***247***: 81–87. https://doi.org/10.1016/j.jmr.2014.08.014.
105. Sato, H., Bottle, S.E., Blinco, J.P., et al. (2008). Electron spin–lattice relaxation of nitroxyl radicals in temperature ranges that span glassy solutions to low-viscosity liquids. J. Magn. Reson. ***191***: 66–77. https://doi.org/10.1016/j.jmr.2007.12.003.
106. Nakagawa, K., Candelaria, M.B., Chik, W.W.C., et al. (1992). Electron-spin relaxation times of chromium(V). J. Magn. Reson. ***98***: 81–91. https://doi.org/10.1016/0022-2364(92)90111-J.
107. Sato, H., Kathirvelu, V., Fielding, A., et al. (2007). Impact of molecular size on electron spin relaxation rates of nitroxyl radicals in glassy solvents between 100 and 300 K. Mol. Phys. ***105***: 2137–2151. https://doi.org/10.1080/00268970701724966.
108. Kathirvelu, V., Eaton, G.R., and Eaton, S.S. (2009). Impact of chlorine substitution on spin–lattice relaxation of triarylmethyl and 1,4-benzosemiquinone radicals in glass-forming solvents between 25 and 295 K. Appl. Magn. Reson. ***37***: 649. https://doi.org/10.1007/s00723-009-0086-3.
109. McNamara, L.E., Zhou, A., Rajh, T., et al. (2023). Realizing solution-phase room temperature quantum coherence in a tetrathiafulvalene-based diradicaloid complex. Cell Rep. Phys. Sci. ***4***: 101693. https://doi.org/10.1016/j.xcrp.2023.101693.
110. Hou, L., Zhang, Y., Zhang, Y., et al. (2024). Tunable quantum coherence of luminescent molecular spins organized via block copolymer self-assembly. Adv. Quantum Technol. 2400064. https://doi.org/10.1002/qute.202400064.
111. Sun, L., Yang, L., Dou, J.-H., et al. (2022). Room-temperature quantitative quantum sensing of lithium ions with a radical-embedded metal–organic framework. J. Am. Chem. Soc. ***144***: 19008–19016. https://doi.org/10.1021/jacs.2c07692.
112. Oanta, A.K., Collins, K.A., Evans, A.M., et al. (2023). Electronic spin qubit candidates arrayed within layered two-dimensional polymers. J. Am. Chem. Soc. ***145***: 689–696. https://doi.org/10.1021/jacs.2c11784.
113. Lu, Y., Hu, Z., Petkov, P., et al. (2024). Tunable charge transport and spin dynamics in two-dimensional conjugated metal–organic frameworks. J. Am. Chem. Soc. ***146***: 2574–2582. https://doi.org/10.1021/jacs.3c11172.
114. Dai, Y.Z., Dong, B.W., Kao, Y., et al. (2018). Chemical modification toward long spin lifetimes in organic conjugated radicals. ChemPhysChem ***19***: 2972–2977. https://doi.org/10.1002/cphc.201800742.
115. Tesi, L., Stemmler, F., Winkler, M., et al. (2023). Modular approach to creating functionalized surface arrays of molecular qubits. Adv. Mater. ***35***: 2208998. https://doi.org/10.1002/adma.202208998.
116. Poryvaev, A.S., Gjuzi, E., Polyukhov, D.M., et al. (2021). Blatter-radical-grafted mesoporous silica as prospective nanoplatform for spin manipulation at ambient conditions. Angew. Chem. Int. Ed. ***60***: 8683–8688. https://doi.org/10.1002/anie.202015058.
117. Biller, J.R., Elajaili, H., Meyer, V., et al. (2013). Electron spin–lattice relaxation mechanisms of rapidly-tumbling nitroxide radicals. J. Magn. Reson. ***236***: 47–56. https://doi.org/10.1016/j.jmr.2013.08.006.

118. Bader, K., Dengler, D., Lenz, S., et al. (2014). Room temperature quantum coherence in a potential molecular qubit. Nat. Commun. ***5***: 5304. https://doi.org/10.1038/ncomms6304.
119. Yamabayashi, T., Atzori, M., Tesi, L., et al. (2018). Scaling up electronic spin qubits into a three-dimensional metal–organic framework. J. Am. Chem. Soc. ***140***: 12090–12101. https://doi.org/10.1021/jacs.8b06733.
120. Urtizberea, A., Natividad, E., Alonso, P.J., et al. (2020). Vanadyl spin qubit 2D arrays and their integration on superconducting resonators. Mater. Horiz. ***7***: 885–897. https://doi.org/10.1039/C9MH01594A.
121. Lunghi, A., and Sanvito, S. (2019). How do phonons relax molecular spins? Sci. Adv. ***5***: eaax7163. https://doi.org/10.1126/sciadv.aax7163.
122. Tesi, L., Lunghi, A., Atzori, M., et al. (2016). Giant spin–phonon bottleneck effects in evaporable vanadyl-based molecules with long spin coherence. Dalton Trans. ***45***: 16635–16643. https://doi.org/10.1039/c6dt02559e.
123. Lunghi, A., Totti, F., Sanvito, S., et al. (2017). Intra-molecular origin of the spin-phonon coupling in slow-relaxing molecular magnets. Chem. Sci. ***8***: 6051–6059. https://doi.org/10.1039/c7sc02832f.
124. Briganti, M., Santanni, F., Tesi, L., et al. (2021). A complete ab initio view of Orbach and Raman spin–lattice relaxation in a dysprosium coordination compound. J. Am. Chem. Soc. ***143***: 13633–13645. https://doi.org/10.1021/jacs.1c05068.
125. Lunghi, A. (2022). Toward exact predictions of spin-phonon relaxation times: an ab initio implementation of open quantum systems theory. Sci. Adv. ***8***: eabn7880. https://doi.org/10.1126/sciadv.abn7880.
126. Garlatti, E., Albino, A., Chicco, S., et al. (2023). The critical role of ultra-low-energy vibrations in the relaxation dynamics of molecular qubits. Nat. Commun. ***14***: 1653. https://doi.org/10.1038/s41467-023-36852-y.
127. Santanni, F., Albino, A., Atzori, M., et al. (2021). Probing vibrational symmetry effects and nuclear spin economy principles in molecular spin qubits. Inorg. Chem. ***60***: 140–151. https://doi.org/10.1021/acs.inorgchem.0c02573.
128. Lunghi, A. (2023). Spin-Phonon Relaxation in Magnetic Molecules: Theory, Predictions and Insights. In Computational Modelling of Molecular Nanomagnets, G. Rajaraman, ed. (Cham: Springer), pp. 219–289. https://doi.org/10.1007/978-3-031-31038-6_6.
129. Stoll, S., and Schweiger, A. (2006). EasySpin, a comprehensive software package for spectral simulation and analysis in EPR. J. Magn. Reson. ***178***: 42–55. https://doi.org/10.1016/j.jmr.2005.08.013.
130. Zecevic, A., Eaton, G.R., Eaton, S.S., et al. (1998). Dephasing of electron spin echoes for nitroxyl radicals in glassy solvents by non-methyl and methyl protons. Mol Phys ***95***: 1255–1263. https://doi.org/10.1080/00268979809483256.
131. Graham, M.J., Yu, C.-J., Krzyaniak, M.D., et al. (2017). Synthetic approach to determine the effect of nuclear spin distance on electronic spin decoherence. J. Am. Chem. Soc. ***139***: 3196–3201. https://doi.org/10.1021/jacs.6b13030.
132. Jain, S.K., Yu, C.-J., Wilson, C.B., et al. (2021). Dynamic nuclear polarization with vanadium(IV) metal centers. Chem ***7***: 421–435. https://doi.org/10.1016/j.chempr.2020.10.021.
133. Kevan, L., and Narayana, P.A. (1979). Disordered matrices. In Multiple Electron Resonance Spectroscopy, M.M. Dorio and J.H. Freed, eds. (Plenum Press), pp. 229–260.
134. Bowman, M.K., and Norris, J.R. (1982). Cross relaxation of free radicals in partially ordered solids. J. Phys. Chem. ***86***: 3385–3390. https://doi.org/10.1021/j100214a024.
135. Gu, L., and Wu, R. (2021). Origin of the anomalously low Raman exponents in single molecule magnets. Phys. Rev. B ***103***: 014401. https://doi.org/10.1103/PhysRevB.103.014401.
136. Gu, L., and Wu, R. (2020). Origins of slow magnetic relaxation in single-molecule magnets. Phys. Rev. Lett. ***125***: 117203. https://doi.org/10.1103/PhysRevLett.125.117203.
137. Fielding, A.J., Carl, P.J., Eaton, G.R., et al. (2005). Multifrequency EPR of four triarylmethyl radicals. Appl. Magn. Reson. ***28***: 231–238. https://doi.org/10.1007/BF03166758.
138. Owenius, R., Eaton, G.R., and Eaton, S.S. (2005). Frequency (250 MHz to 9.2 GHz) and viscosity dependence of electron spin relaxation of triarylmethyl radicals at room temperature. J. Magn. Reson. ***172***: 168–175. https://doi.org/10.1016/j.jmr.2004.10.007.
139. Mirzoyan, R., Kazmierczak, N.P., and Hadt, R.G. (2021). Deconvolving contributions to decoherence in molecular electron spin qubits: A dynamic ligand field approach. Chem. Eur J. ***27***: 9482–9494. https://doi.org/10.1002/chem.202100845.
140. Rengan, S.K., Khakhar, M.P., Prabhananda, B.S., et al. (1974). Study of molecular motions in liquids by electron spin-lattice relaxation measurements, I: Semiquinone ions in hydrogen bonding solvents. Pramana - J. Phys. ***3***: 95–121. https://doi.org/10.1007/BF02847118.
141. Biller, J.R., Meyer, V., Elajaili, H., et al. (2011). Relaxation times and line widths of isotopically-substituted nitroxides in aqueous solution at X-band. J. Magn. Reson. ***212***: 370–377. https://doi.org/10.1016/j.jmr.2011.07.018.
142. Biller, J.R., McPeak, J.E., Eaton, S.S., et al. (2018). Measurement of T_{1e}, T_{1N}, T_{1HE}, T_{2e}, and T_{2HE} by pulse EPR at X-band for nitroxides at concentrations relevant to solution DNP. Appl. Magn. Reson. ***49***: 1235–1251. https://doi.org/10.1007/s00723-018-1049-3.
143. Degen, C.L., Reinhard, F., and Cappellaro, P. (2017). Quantum sensing. Rev. Mod. Phys. ***89***: 035002. https://doi.org/10.1103/RevModPhys.89.035002.
144. Pei, L., and Hong-ying, Y. (2018). Comparison of longitudinal relaxation time measured by inversion recovery method and saturation recovery method. Phys. Exp. ***38***: 11–14. https://doi.org/10.19655/j.cnki.1005-4642.2018.12.003.
145. Becker, E.D., Ferretti, J.A., Gupta, R.K., et al. (1980). The choice of optimal parameters for measurement of spin-lattice relaxation times. ii. Comparison of saturation recovery, inversion recovery, and fast inversion recovery experiments. J. Magn. Reson. ***37***: 381–394. https://doi.org/10.1016/0022-2364(80)90045-1.
146. Abobeih, M.H., Cramer, J., Bakker, M.A., et al. (2018). One-second coherence for a single electron spin coupled to a multi-qubit nuclear-spin environment. Nat. Commun. ***9***: 2552. https://doi.org/10.1038/s41467-018-04916-z.
147. Dai, Y., Fu, Y., Shi, Z., et al. (2021). Experimental protection of the spin coherence of a molecular qubit exceeding a millisecond. Chin. Phys. Lett. ***38***: 030303. https://doi.org/10.1088/0256-307X/38/3/030303.
148. Lombardi, F., Tsang, M.-Y., Segantini, M., et al. (2022). Room-Temperature coherence boosting of molecular graphenoids by environmental spectral decomposition. Phys. Rev. B ***105***: 094106. https://doi.org/10.1103/PhysRevB.105.094106.
149. Harbridge, J.R., Eaton, S.S., and Eaton, G.R. (2003). Comparison of electron spin relaxation times measured by Carr–Purcell–Meiboom–Gill and two-pulse spin-echo sequences. J. Magn. Reson. ***164***: 44–53. https://doi.org/10.1016/s1090-7807(03)00182-4.
150. de Lange, G., Wang, Z.H., Ristè, D., et al. (2010). Universal dynamical decoupling of a single solid-state spin from a spin bath. Science ***330***: 60–63. https://doi.org/10.1126/science.1192739.
151. Wang, F., Zu, C., He, L., et al. (2016). Experimental realization of robust dynamical decoupling with bounded controls in a solid-state spin system. Phys. Rev. B ***94***: 064304. https://doi.org/10.1103/PhysRevB.94.064304.
152. Souza, A.M., Álvarez, G.A., and Suter, D. (2012). Robust dynamical decoupling. Philos. Trans. A Math. Phys. Eng. Sci. ***370***: 4748–4769. https://doi.org/10.1098/rsta.2011.0355.
153. Moore, W. (2021). EPR relaxation of modified triphenylmethyl and nitroxide radicals. Graduate Studies thesis (University of Denver).
154. Manenkov, A.A., and Prokhorov, A.M. (1970). Spin-Lattice relaxation and cross-relaxation interactions in chromium corundum. In The Solid State Maser, J.W. Orton, D.H. Paxman, and J.C. Walling, eds. (Pergamon Press), pp. 168–183.
155. Segawa, T.F., Doll, A., Pribitzer, S., et al. (2015). Copper ESEEM and HYSCORE through ultra-wideband chirp EPR spectroscopy. J. Chem. Phys. ***143***: 044201. https://doi.org/10.1063/1.4927088.
156. Bujak, P., Kulszewicz-Bajer, I., Zagorska, M., et al. (2013). Polymers for electronics and spintronics. Chem. Soc. Rev. ***42***: 8895–8999. https://doi.org/10.1039/c3cs60257e.
157. Uddin, M.A., Yu, H., Wang, L., et al. (2020). Recent progress in EPR study of spin labeled polymers and spin probed polymer systems. J. Polym. Sci. ***58***: 1924–1948. https://doi.org/10.1002/pol.20200039.
158. Pachfule, P., Acharjya, A., Roeser, J., et al. (2019). Donor–acceptor covalent organic frameworks for visible light induced free radical polymerization. Chem. Sci. ***10***: 8316–8322. https://doi.org/10.1039/c9sc02601k.
159. Wu, S., Li, M., Phan, H., et al. (2018). Toward Two-dimensional π-conjugated covalent organic radical frameworks. Angew. Chem. Int. Ed. ***57***: 8007–8011. https://doi.org/10.1002/anie.201801998.
160. Su, J., Xu, N., Murase, R., et al. (2021). Persistent radical tetrathiafulvalene-based 2D metal-organic frameworks and their application in efficient photothermal conversion. Angew. Chem. Int. Ed. ***60***: 4789–4795. https://doi.org/10.1002/anie.202013811.
161. Chen, X., Xie, H., Lorenzo, E.R., et al. (2022). Direct observation of modulated radical spin states in metal–organic frameworks by controlled flexibility. J. Am. Chem. Soc. ***144***: 2685–2693. https://doi.org/10.1021/jacs.1c11417.
162. Jellen, M.J., Ayodele, M.J., Cantu, A., et al. (2020). 2D arrays of organic qubit candidates embedded into a pillared-paddlewheel metal–organic framework. J. Am. Chem. Soc. ***142***: 18513–18521. https://doi.org/10.1021/jacs.0c07251.
163. Joo, Y., Agarkar, V., Sung, S.H., et al. (2018). A nonconjugated radical polymer glass with high electrical conductivity. Science ***359***: 1391–1395. https://doi.org/10.1126/science.aao7287.
164. Nesvadba, P., Bugnon, L., Maire, P., et al. (2010). Synthesis of a novel spirobisnitroxide polymer and its evaluation in an organic radical battery. Chem. Mater. ***22***: 783–788. https://doi.org/10.1021/cm901374u.
165. Wang, S., Park, A.M.G., Flouda, P., et al. (2020). Solution-Processable thermally crosslinked organic radical polymer battery cathodes. ChemSusChem ***13***: 2371–2378. https://doi.org/10.1002/cssc.201903554.
166. Layer, G., Heinz, D.W., Jahn, D., et al. (2004). Structure and function of radical SAM enzymes. Curr. Opin. Chem. Biol. ***8***: 468–476. https://doi.org/10.1016/j.cbpa.2004.08.001.
167. Broderick, J.B., Broderick, W.E., and Hoffman, B.M. (2023). Radical SAM enzymes: nature's choice for radical reactions. FEBS Lett. ***597***: 92–101. https://doi.org/10.1002/1873-3468.14519.
168. Nicolet, Y. (2020). Structure–function relationships of radical SAM enzymes. Nat. Catal. ***3***: 337–350. https://doi.org/10.1038/s41929-020-0448-7.
169. Wang, X., Guo, R., Xu, D., et al. (2015). Anisotropic lattice thermal conductivity and suppressed acoustic phonons in MOF-74 from first principles. J. Phys. Chem. C ***119***: 26000–26008. https://doi.org/10.1021/acs.jpcc.5b08675.
170. Bhogra, M., and Waghmare, U.V. (2021). Flat phonon band-based mechanism of amorphization of MOF-5 at ultra-low pressures. J. Phys. Chem. C ***125***: 14924–14931. https://doi.org/10.1021/acs.jpcc.1c02598.
171. Kumar, S., Kamaraju, N., Karthikeyan, B., et al. (2010). Terahertz spectroscopy of single-walled carbon nanotubes in a polymer film: observation of low-frequency phonons. J. Phys. Chem. C ***114***: 12446–12450. https://doi.org/10.1021/JP103105H.
172. Hou, L., Xu, H., Zhang, X., et al. (2022). Impact of polymer rigidity on the thermoresponsive luminescence and electron spin resonance of polyester-tethered single radicals. Macromolecules ***55***: 8619–8628. https://doi.org/10.1021/acs.macromol.2c01199.
173. Kato, K., Kimura, S., Kusamoto, T., et al. (2019). Luminescent radical-excimer: excited-state dynamics of luminescent radicals in doped host crystals. Angew. Chem. Int. Ed. ***58***: 2606–2611. https://doi.org/10.1002/anie.201813479.

174. Sarfo, D.K., Izake, E.L., O'Mullane, A.P., et al. (2019). Fabrication of nanostructured SERS substrates on conductive solid platforms for environmental application. Crit. Rev. Environ. Sci. Technol. ***49***: 1294–1329. https://doi.org/10.1080/10643389.2019.1576468.
175. Tan, K.T., Ghosh, S., Wang, Z., et al. (2023). Covalent organic frameworks. Nat. Rev. Methods Primers ***3***: 1–19. https://doi.org/10.1038/s43586-022-00181-z.
176. Furukawa, H., Cordova, K.E., O'Keeffe, M., et al. (2013). The chemistry and applications of metal-organic frameworks. Science ***341***: 1230444. https://doi.org/10.1126/science.1230444.
177. Yu, C.-J., Krzyaniak, M.D., Fataftah, M.S., et al. (2019). A concentrated array of copper porphyrin candidate qubits. Chem. Sci. ***10***: 1702–1708.
178. Yu, C.-J., von Kugelgen, S., Krzyaniak, M.D., et al. (2020). Spin and phonon design in modular arrays of molecular qubits. Chem. Mater. ***32***: 10200–10206.
179. Jhulki, S., Feriante, C.H., Mysyk, R., et al. (2021). A naphthalene diimide covalent organic framework: comparison of cathode performance in lithium-ion batteries with amorphous cross-linked and linear analogues, and its use in aqueous lithium-ion batteries. ACS Appl. Energy Mater. ***4***: 350–356.
180. Evans, A.M., Collins, K.A., Xun, S., et al. (2022). Controlled n-doping of naphthalene-diimide-based 2D polymers. Adv. Mater. ***34***: e2101932. https://doi.org/10.1002/adma.202101932.
181. Narayan, T.C., Miyakai, T., Seki, S., et al. (2012). High charge mobility in a tetrathiafulvalene-based microporous metal–organic framework. J. Am. Chem. Soc. ***134***: 12932–12935.
182. Lenz, S., Kern, B., Schneider, M., et al. (2019). Measurement of quantum coherence in thin films of molecular quantum bits without post-processing. Chem. Commun. ***55***: 7163–7166.
183. Nielsen, M.A., and Chuang, I.L. (2010). Quantum Computation and Quantum Information, 10th Anniversary Edition (Cambridge University Press). https://doi.org/10.1017/CBO9780511976667.
184. Shor, P.W. (1994). Algorithms for quantum computation: discrete logarithms and factoring. In Proceedings 35th Annual Symposium on Foundations of Computer Science, pp. 124–134.
185. Barenco, A., Bennett, C.H., Cleve, R., et al. (1995). Elementary gates for quantum computation. Phys. Rev. ***52***: 3457–3467.
186. Zhao, P., Xu, P., Lan, D., et al. (2020). Switchable next-nearest-neighbor coupling for controlled two-qubit operations. Phys. Rev. Appl. ***14***: 064016. https://doi.org/10.1103/PhysRevApplied.14.064016.
187. Khan, J., and Akram, J. (2023). Noise-tolerant superconducting gates with high fidelity. J. Russ. Laser Res. ***44***: 135–147.
188. Lenz, S., König, D., Hunger, D., et al. (2021). Room-Temperature quantum memories based on molecular electron spin ensembles. Adv. Mater. ***33***: 2101673. https://doi.org/10.1002/adma.202101673.
189. Lvovsky, A.I., Sanders, B.C., and Tittel, W. (2009). Optical quantum memory. Nat. Photonics ***3***: 706–714. https://doi.org/10.1038/nphoton.2009.231.
190. Hedges, M.P., Longdell, J.J., Li, Y., et al. (2010). Efficient quantum memory for light. Nature ***465***: 1052–1056. https://doi.org/10.1038/nature09081.
191. Jing, B., Wang, X.-J., Yu, Y., et al. (2019). Entanglement of three quantum memories via interference of three single photons. Nat. Photonics ***13***: 210–213. https://doi.org/10.1038/s41566-018-0342-x.
192. Lago-Rivera, D., Grandi, S., Rakonjac, J.V., et al. (2021). Telecom-heralded entanglement between multimode solid-state quantum memories. Nature ***594***: 37–40. https://doi.org/10.1038/s41586-021-03481-8.
193. Yu, Y., Ma, F., Luo, X.-Y., et al. (2020). Entanglement of two quantum memories via fibres over dozens of kilometres. Nature ***578***: 240–245. https://doi.org/10.1038/s41586-020-1976-7.
194. de Riedmatten, H., Afzelius, M., Staudt, M.U., et al. (2008). A solid-state light–matter interface at the single-photon level. Nature ***456***: 773–777. https://doi.org/10.1038/nature07607.
195. Bonizzoni, C., Ghirri, A., Santanni, F., et al. (2024). Quantum sensing of magnetic fields with molecular spins. npj Quant. Inf. ***10***: 41. https://doi.org/10.1038/s41534-024-00838-5.
196. Li, T., and Yin, Z.-Q. (2016). Quantum superposition, entanglement, and state teleportation of a microorganism on an electromechanical oscillator. Sci. Bull. ***61***: 163–171. https://doi.org/10.1007/s11434-015-0990-x.
197. Cai, J., and Plenio, M.B. (2013). Chemical compass model for avian magnetoreception as a quantum coherent device. Phys. Rev. Lett. ***111***: 230503. https://doi.org/10.1103/PhysRevLett.111.230503.
198. Hore, P.J., and Mouritsen, H. (2016). The radical-pair mechanism of magnetoreception. Annu. Rev. Biophys. ***45***: 299–344. https://doi.org/10.1146/annurev-biophys-032116-094545.
199. Xie, C. (2022). Searching for unity in diversity of animal magnetoreception: from biology to quantum mechanics and back. Innovation ***3***: 100229. https://doi.org/10.1016/j.xinn.2022.100229.
200. Zhou, L., Yang, W., Ji, S., et al. (2024). Spin manipulation in organic radicals. The Innovation Materials ***2***: 100052. https://doi.org/10.59717/j.xinn-mater.2024.100052.
201. Qiu, Y., Equbal, A., Lin, C., et al. (2023). Optical spin polarization of a narrow linewidth electron spin qubit in a chromophore/stable-radical system. Angew. Chem. Int. Ed. ***62***: e202214668. https://doi.org/10.1002/anie.202214668.
202. Tuorila, J., Partanen, M., Ala-Nissila, T., et al. (2017). Efficient protocol for qubit initialization with a tunable environment. npj Quant. Inf. ***3***: 27. https://doi.org/10.1038/s41534-017-0027-1.
203. Du, J., Shi, F., Kong, X., et al. (2024). Single-molecule scale magnetic resonance spectroscopy using quantum diamond sensors. Rev. Mod. Phys. ***96***: 025001. https://doi.org/10.1103/RevModPhys.96.025001.
204. Jansen, R., and Yuasa, S. (2024). High temperature spin selectivity in a quantum dot qubit using reservoir spin accumulation. Inform ***10***: 21. https://doi.org/10.1038/s41534-024-00815-y.
205. Liu, Y., and Luo, J. (2022). Zoo of silicon-based quantum bits. Innovation ***3***: 100330. https://doi.org/10.1016/j.xinn.2022.100330.
206. Wang, Z., Balembois, L., Rančić, M., et al. (2023). Single-electron spin resonance detection by microwave photon counting. Nature ***619***: 276–281. https://doi.org/10.1038/s41586-023-06097-2.
207. Chiesa, A., Privitera, A., Macaluso, E., et al. (2023). Chirality-Induced spin selectivity: an enabling technology for quantum applications. Adv. Mater. ***35***: e2300472. https://doi.org/10.1002/adma.202300472.

ACKNOWLEDGMENTS

This work was supported by the National Natural Science Foundation of China (no. 22273078) and Hangzhou Municipal Funding, Team of Innovation (TD2022004). We thank Ji Wang for proofreading and polishing.

AUTHOR CONTRIBUTIONS

A.Z. and Z.S. wrote the manuscript. L.S. organized, revised, and supervised the manuscript. All authors contributed to the article and approved the submitted version.

DECLARATION OF INTERESTS

The authors declare no competing interests.

SUPPLEMENTAL INFORMATION

It can be found online at https://doi.org/10.1016/j.xinn.2024.100662.

LEAD CONTACT WEBSITE

https://sunlei.lab.westlake.edu.cn/.

The Innovation, Volume *5*

Supplemental Information

Stable organic radical qubits and their applications in quantum information science

Aimei Zhou, Zhecheng Sun, and Lei Sun

The Innovation

Supplemental Information

Table of Contents

Triphenylmethyl radicals

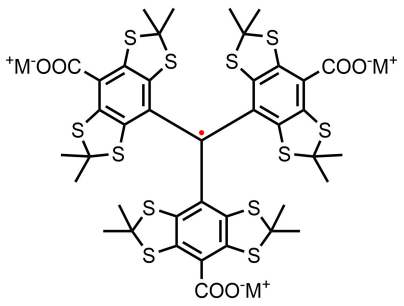

Trityl-CH_3

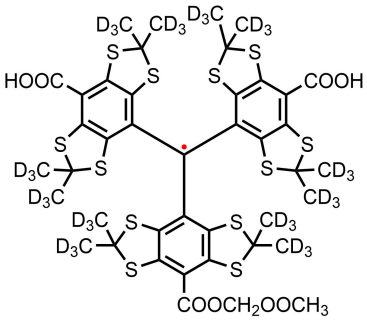

$FDAM_1$

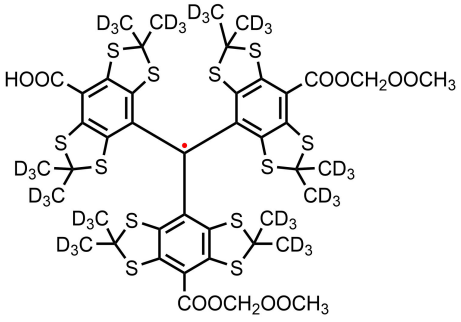

$FDAM_2$

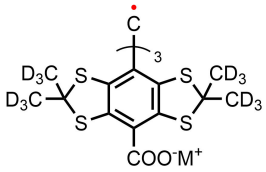

Trityl-CD_3

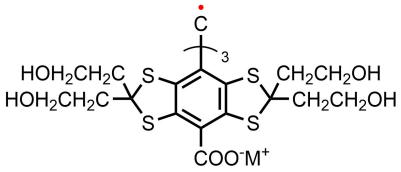

OX63

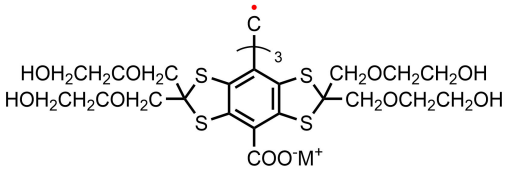

OX31

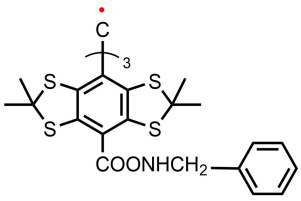

FBA_3

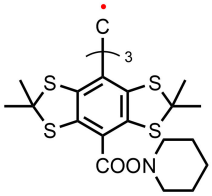

FP_3

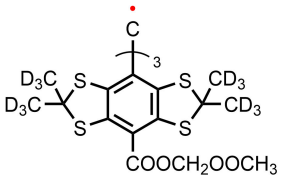

$FDAM_3$

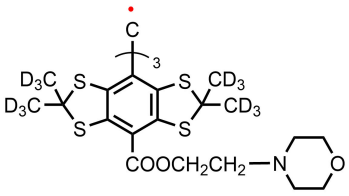

$FDME_3$

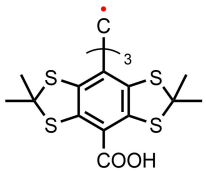

Finland trityl

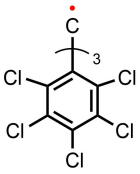

PCTM

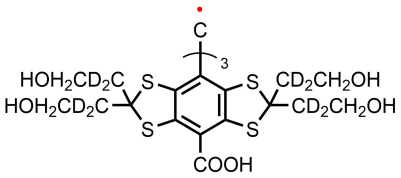

OX63D

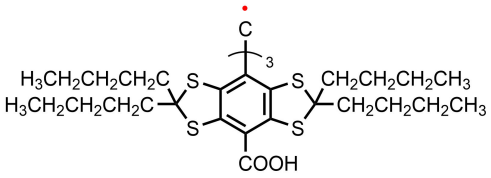

DBHT

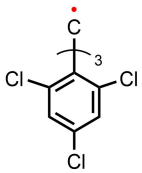

3CM

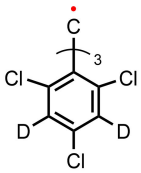

D3CM

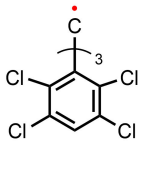

4CM

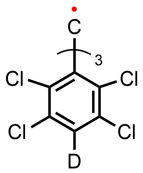

D4CM

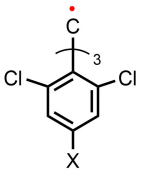

TTM-3BZ-PCL-$PDLLA_m$

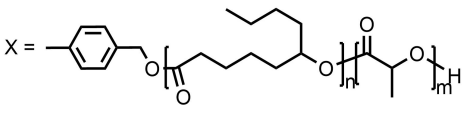

Figure S1. Schemes of triphenylmethyl radicals

Nitroxide radicals

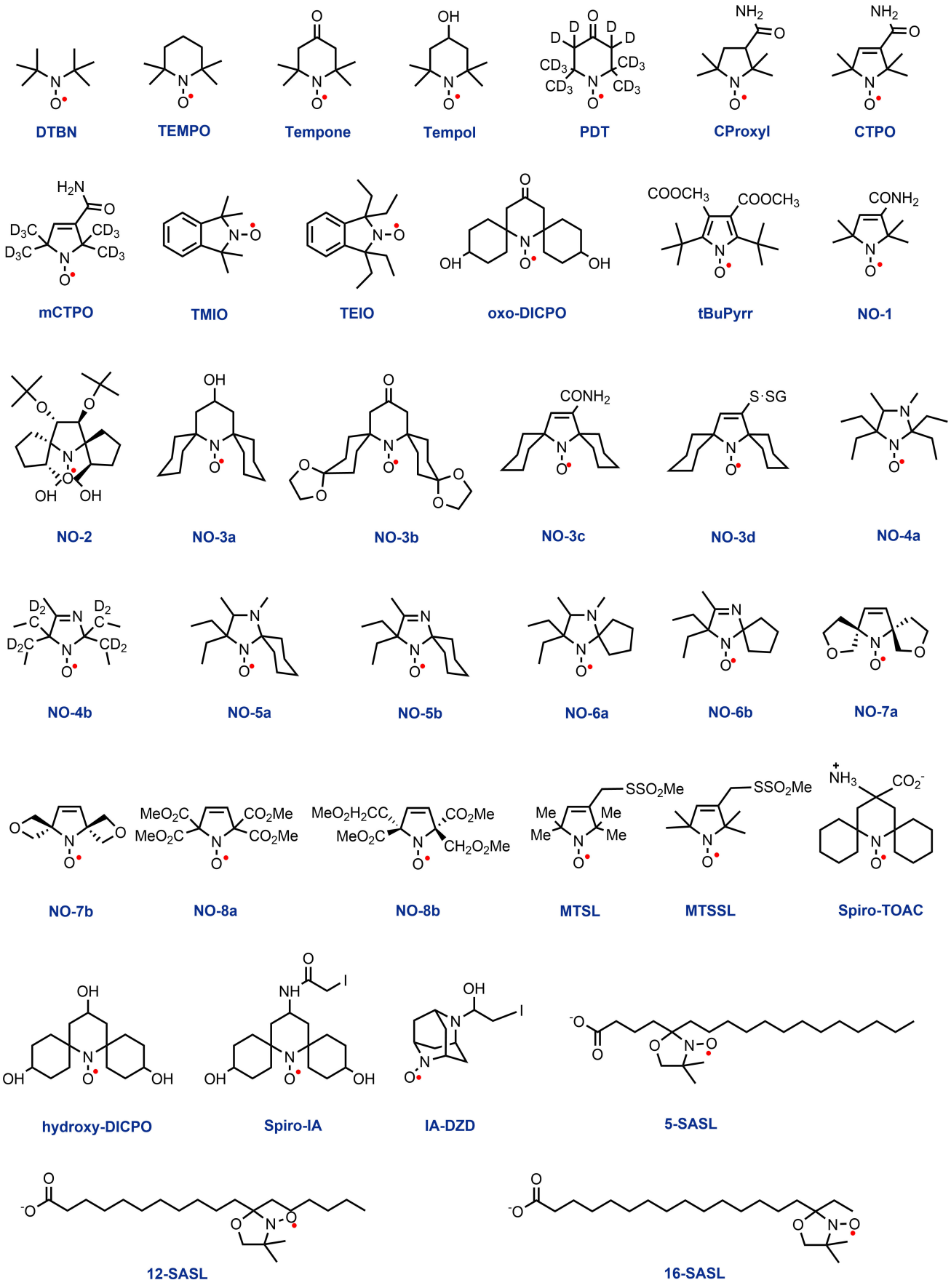

Figure S2. Schemes of nitroxide radicals

Semiquinone radicals

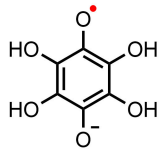

THSQ

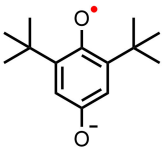

2,6-DTBSQ

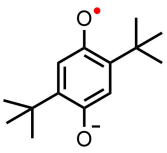

2,5-DTBSQ

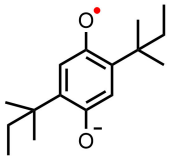

2,5-TASQ

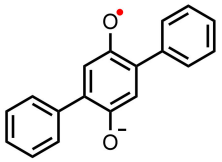

2,5-PSQ

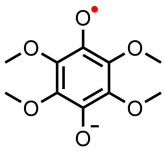

TMBSQ

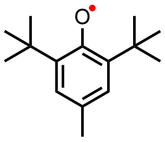

TTBP

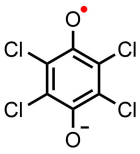

TCSQ

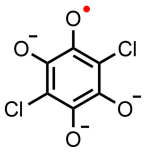

DDBSQ

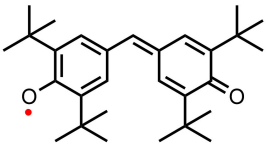

Galvinoxyl

Macrocyclic conjugated radicals

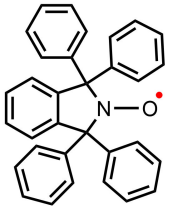

TPHIO

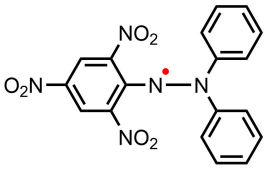

DPPH

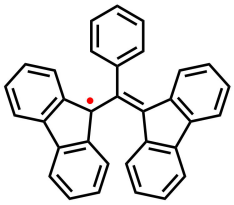

BDPA

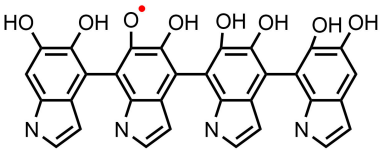

PDA

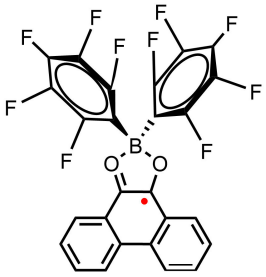

$(C_6F_5)_2B(O_2C_{14}H_8)$

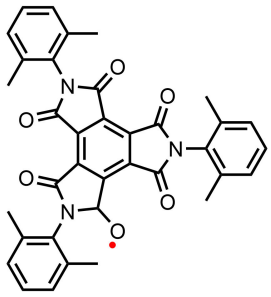

BTI-xy

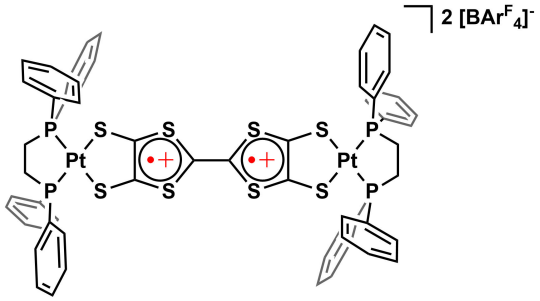

PtTTFtt

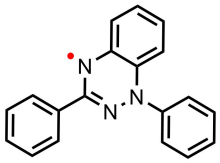

BTR

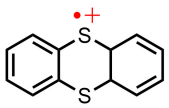

Thianthrene

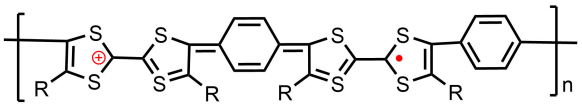

PTTF

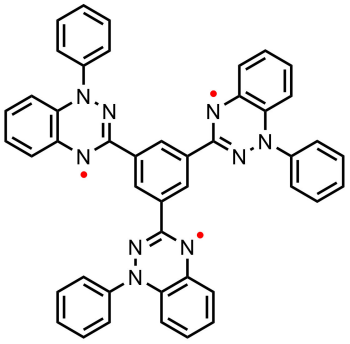

BTR-C_3

Figure S3. Scheme of semiquinone radicals and macrocyclic conjugated radicals

Graphene nanoribbons (GNRs) and carbon nanotubes

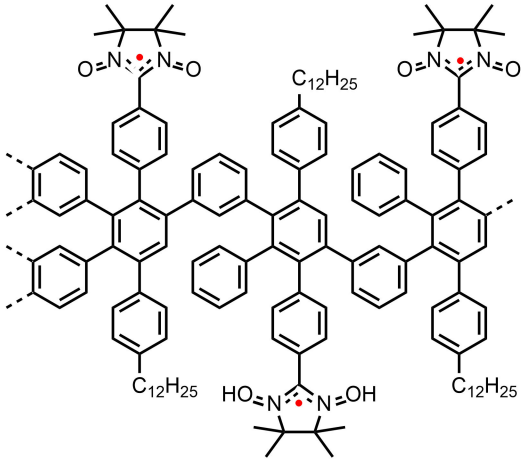

NIT-polyphenylene

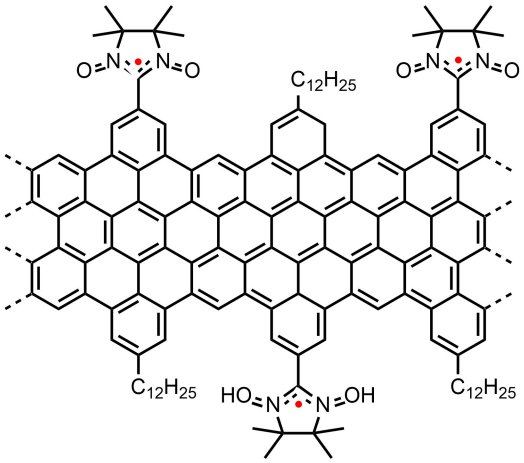

NIT-GNRs

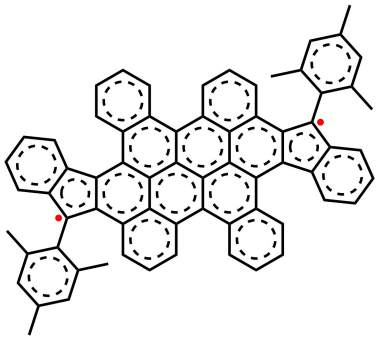

GNRs-1

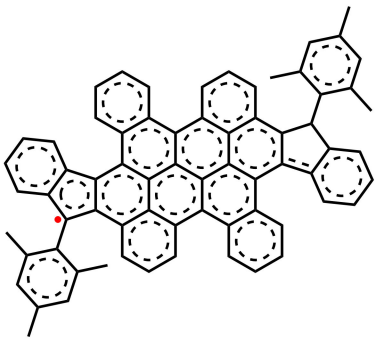

GNRs-2

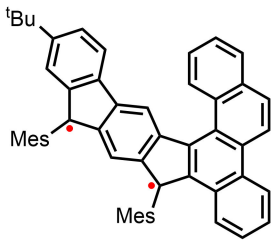

GNRs-3

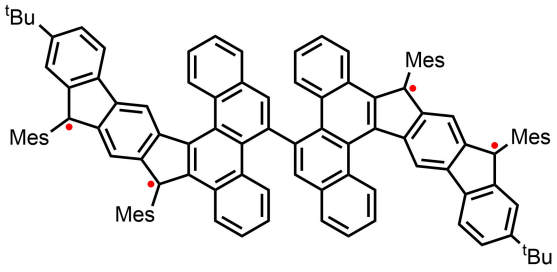

GNRs-4

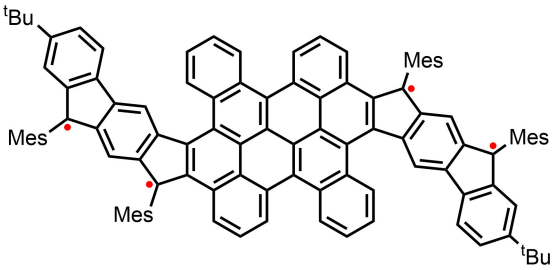

GNRs-5

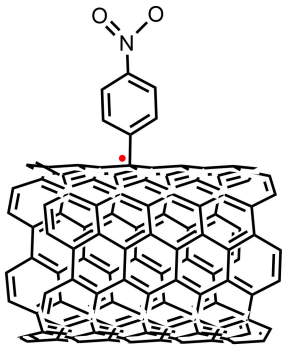

NO_2Ph-SWCNTs

Figure S4. Radicals based on graphene nanoribbons and carbon nanotubes

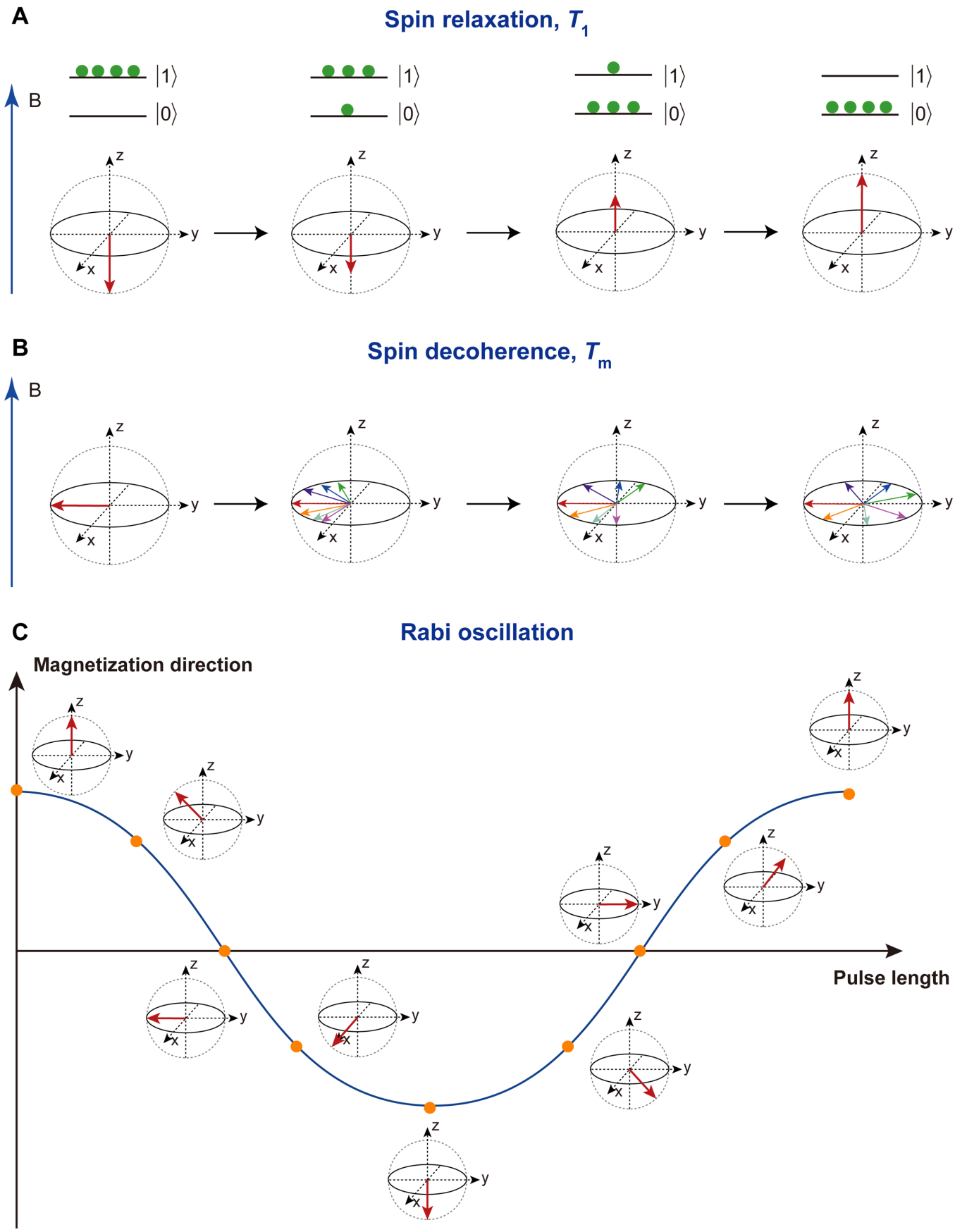

Figure S5. Bloch sphere illustrations of spin dynamics and spin manipulation (A) Spin relaxation process described by T_1. Green dots represent partitions of electron spins on $|0\rangle$ and $|1\rangle$ spin states. The blue arrow on the left marked with "B" represents the external magnetic field. (B) Spin decoherence process described by T_m. (C) Rabi oscillation.

Characterization methods for T_1, T_m, and Rabi oscillations

Radical qubit characterization, including T_1, T_m, and manipulability, relies on pulse electron paramagnetic resonance (EPR) spectroscopy. Pulse EPR spectroscopy initializes the electron spin using a static magnetic field via the Zeeman effect, manipulates it with transient oscillatory magnetic fields generated by a sequence of microwave pulses, and reads out the final state through free induction decays or spin echoes. T_1 could be measured by inversion recovery or saturation recovery pulse sequences, which transform the spin to a nonequilibrium state and monitor the relaxation process (Figure S6C, D). T_m is most often characterized by a Hahn echo decay pulse sequence that generates a superposition state and monitors its decoherence during a free evolution period (Figure S6A).[1,2] T_m may be improved by dynamical decoupling strategies that suppress the influence of environmental magnetic noise.[3,4] The manipulability is demonstrated via Rabi oscillations, which show an oscillatory relationship between superposition and the duration of a nutation pulse (Figure S5C).[5] Practically, molecules displaying quantum coherence always show Rabi oscillations in nutation experiments (Figure S6B). Thus, a radical that exhibits long T_1 and T_m could be qualified as a qubit.[1,2]

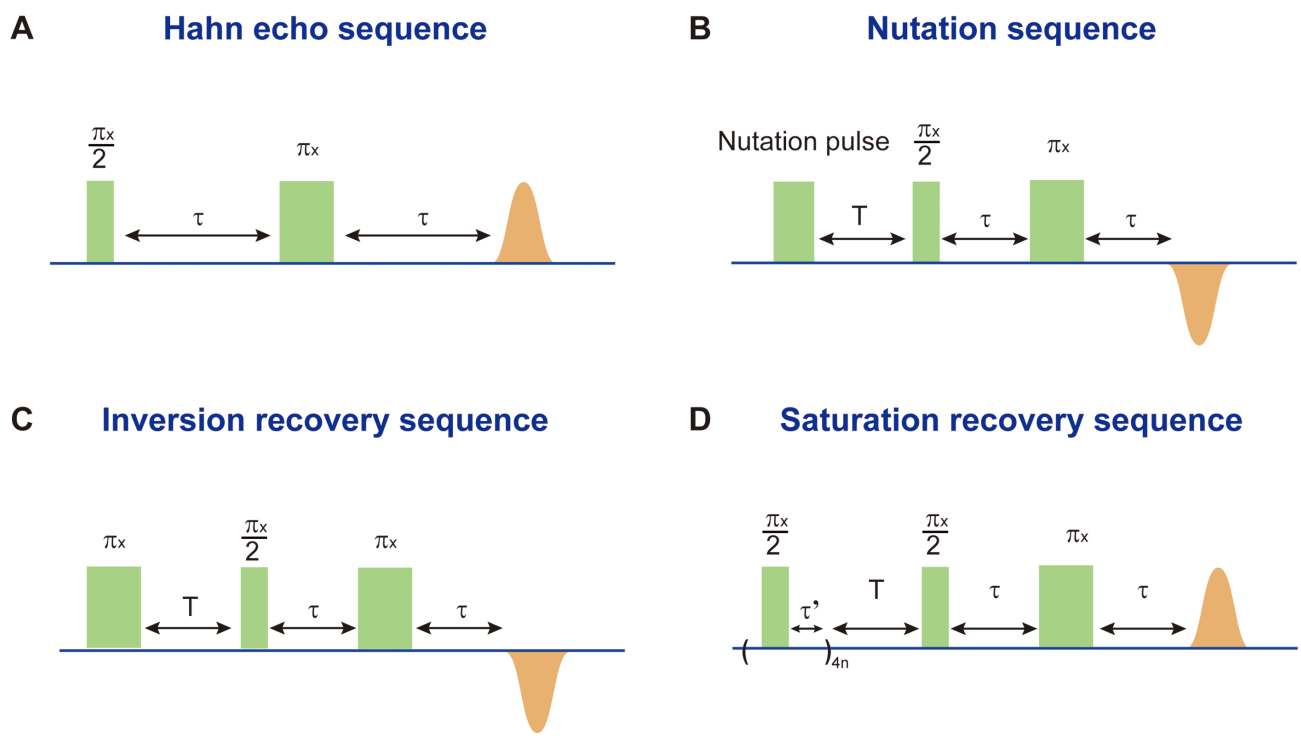

Figure S6. Schemes of pulse sequences (A) Hahn echo sequence. (B) Nutation sequence. (C) Inversion recovery sequence. (D) Saturation recovery sequence. Green rectangles represent pulses whose turning angles are marked above them, and orange objects represent spin echoes.

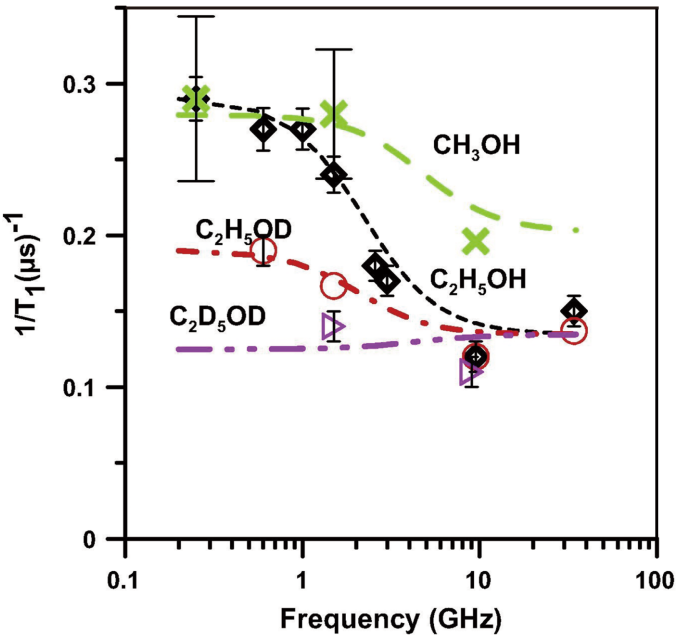

Figure S7. Influence of solvent deuteration on $1/T_1$ (Reproduced from Ref. [6] with the permission from Elsevier, copyright 2014)

Influence of the Larmor frequency on the electron spin dynamics of stable organic radical qubits

The Larmor frequency (ω) describes the frequency of spin precession in an external magnetic field (B), which reflects the Zeeman splitting (E_Z) dictated by the g-factor of spin system and the change of spin state (ΔS),

$$E_Z = \hbar\omega = g\mu_B B\Delta S$$

where $\hbar$ is the reduced Planck constant, μ_B is the Bohr magneton, and ΔS is +1 for an organic mono-radical. In typical EPR experiments, ω is fixed within a narrow range of frequency to match the resonant frequency of the microwave cavity. The resonant frequency is conventionally represented by the microwave band of the EPR instrument, with L-band centered at 1 GHz, S-band 3.5 GHz, X-band 9.8 GHz, Q-band 34 GHz, and W-band 94 GHz.

Electron spins with different Larmor frequencies might couple with different phonon modes, which in turn affects spin relaxation processes. Raman, Orbach, and local-mode processes typically involve phonons whose frequencies are well above the Larmor frequency of spin, so these processes are frequency-independent.[1,2] In contrast, direct and thermally activated processes that involve low-frequency phonons typically show significant frequency dependence. The former monotonically increases with rising Larmor frequency, whereas the latter has a maximum value that appears when $\omega\tau_c = 1$ where τ_c is the correlation time of the thermally activated process.[7,8] For example, for a nitroxide radical, PDT (Figure S2), dissolved in a mixture of water and glycerol, $\tau_c = 1.0 \times 10^{-10}\ s$. Hence, the thermally activated process is the most pronounced at the frequency $\nu = \frac{\omega}{2\pi} = 1.6\ GHz$. This is in good agreement with the experimental observation where $1/T_1$ shows the maximum at 1.5 GHz (Figure S8B).[7]

As discussed in the main text, spin relaxation processes in fluid solution mainly include tumbling-induced spin rotation and modulation of anisotropic interactions comprising of g-anisotropy, A-anisotropy, and dipolar coupling with solvent nuclei.[1] According to the corresponding equation in Table S1, the spin rotation is independent of the Larmor frequency (Figure 5A), yet others are frequency-dependent (Figure 5B–D) and their salience is related to the tumbling correlation time (τ_R). For instance, Biller et al. acquired the room-temperature T_1 of a series of nitroxide radicals at various frequencies (250 MHz to 34 GHz) in solutions whose τ_R values range from 4 to 50 ps.[8] Take the PDT radical (Figure S2) as an example. When τ_R is 4 ps, the spin relaxation is predominantly governed by spin rotation, rendering T_1 independent of frequency (T_1 = 1.05 − 1.18 μs; Figure S8A). In contrast, as τ_R exceeds 15 ps, the dominant process shifts towards g- and A-anisotropy modulations. Meanwhile, the thermally activated process exerts its most substantial influence on T_1 within the frequency range of 1 − 2 GHz. Consequently, as τ_R increases, the frequency-dependence of T_1 becomes more and more salient. For example, when τ_R is 50 ps, T_1 drops from approximately 4.5 μs at 250 MHz to approximately 0.28 μs at 34 GHz.[7]

The frequency-dependence of T_m remains unclear. Shi *et al* found that the T_m of triphenylmethyl radicals only shows weak frequency-dependence within the range of 250 MHz – 1.5 GHz.[9] Biller *et al* showed that nitroxide radicals exhibit decreasing T_m with increasing frequency from 250 MHz to 34 GHz.[7] In contrast, Ghim *et al* observed that within the range of 1.8 – 19.4 GHz, the T_m of irradiated L- alanine radicals increases with increasing frequency.[10] From these observations, it seems that the frequency dependence of T_m may be different for different radicals and/or frequency ranges. A comprehensive and in-depth investigation into this phenomenon is needed.

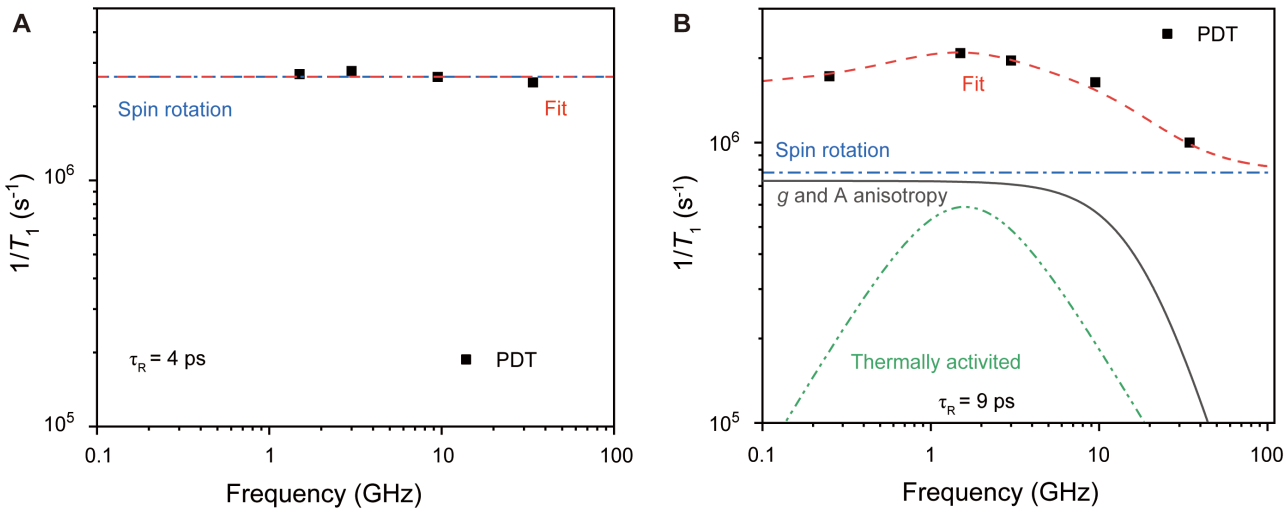

Figure S8. Influence of Larmor frequency on spin dynamics Frequency dependence of $1/T_1$ for PDT in solvents whose τ_R being (A) 4 ps and (B) 9 ps, respectively. Data used for these two simulations (black squares) are extracted from Ref[8] for (A) and Ref[7] for (B).

Table S1. The equation of typical spin relaxation mechanisms[1,11,12]

Mechanism	Equation
Direct	$A_{Dir} B^4 \frac{e^{\hbar\omega/k_B T}}{e^{\hbar\omega/k_B T}-1}$
Raman	$A_{Ram}\left(\frac{T}{\Theta_D}\right)^9 \int_0^{\frac{\Theta_D}{T}} x^8 \frac{e^x}{(e^x-1)^2} dx$ (sometimes $A_{Ram} T^m$ with $m = 2-9$)
Orbach	$A_{Orb} \frac{\Delta^3}{e^{\Delta/k_B T}-1}$
Local mode	$A_{loc} \frac{e^{\hbar\omega_{phonon}/k_B T}}{\left(e^{\hbar\omega_{phonon}/k_B T}-1\right)^2}$
Thermally activated	$A_{therm} \frac{2\tau_c^0 e^{E_a/k_B T}}{1+\omega^2 {\tau_c^0}^2 e^{2E_a/k_B T}}$
Tumbling-dependent	$\frac{\sum_{i=x,y,z}(g_i - g_e)^2}{9\tau_R} + \frac{2}{5}\left(\frac{\mu_B \omega}{g\beta}\right)^2 \left\{\frac{(\Delta g)^2}{3} + (\delta g)^2\right\} J(\omega)$ $+ \frac{2}{9} I(I+1) \sum_i (A_i - a_{iso})^2 J(\omega) + C_{solvent} \frac{\tau_{solvent}}{1+(\omega\tau_{solvent})^2}$
Cross relaxation	constant (temperature-independent)

T: temperature; B: magnetic field strength; ω: Larmor frequency; Θ_D: Debye temperature; Δ: energy of low-lying excited state; ω_{phonon}: energy of local phonon mode. τ_c^0: pre-exponential factor; E_a: activation energy; g_i: principle *g* value along the *i* axis; g_e: *g* value of free electron; τ_R: tumbling correlation time; μ_B: Bohr magneton; $\Delta g = g_{zz} - 0.5(g_{xx}+g_{yy})$; $\delta g = 0.5(g_{xx}-g_{yy})$; $J(\omega) = \frac{\tau_R}{1+(\omega\tau_R)^2}$; I: nuclear spin; A_i: principle component of the nuclear hyperfine constant along the *i* axis in angular frequency units; a_{iso}: the isotropic nuclear hyperfine constant; $\tau_{solvent}$: correlation time for motion of the solvent relative to the radical; $C_{solvent}$: a function of the dipolar interaction with solvent nuclei. A_{Dir}, A_{Ram}, A_{Orb}, A_{loc}, A_{therm} are pre-factors.

Table S2. T_1 and T_m of stable organic radical qubits

Radical[a]	Concentration / mmol·L^{-1}	Frequency / GHz	Solvent	Temperature / K	T_1 / μs	T_m / μs	Reference
Trityl-CH_3	0.2	9.5	H_2O : glycerol = 1:1	100	1060	3.9	[13]
				294	16	2.2	[14]
			H_2O : glycerol = 1:9	294	17	0.18	
			H_2O	294	15	8.7	
		95	H_2O : glycerol = 1:1	100	838	3.1	[13]
Trityl-CD_3	0.2	9.5	H_2O : glycerol = 1:1	100	955	4.8	[13]
				294	17	3.7	[14]
			H_2O : glycerol = 1:9	294	19	0.24	
			H_2O	294	17	11	
		95	H_2O : glycerol = 1:1	100	756	4.5	[13]
		1.5	H_2O : glycerol = 1:1	294	15	4.2	[14]
			H_2O : glycerol = 1:9	294	18	0.21	
			H_2O	294	14	12.5	
		3.1	H_2O : glycerol = 1:1	294	16	3.8	
			H_2O	294	16	13	
Finland trityl	2.5	9.5	H_2O : glycerol = 4:6	77	1670[b]	NA[c]	[15]
		95			1100[b]		
OX63	0.2	9.5	H_2O : glycerol = 1:1	100	1200	5.1	[13]
		95			979	4.5	[13]
OX31	0.2	9.5	H_2O : glycerol = 1:1	100	1360	5.0	[13]
		95			1042	4.4	[13]
$FDAM_1$	NA[c]	9.5	MeOH	300	14.3	7.6	[16]
		34			12.6	2.8	
		9.5	H_2O	300	14.5	10.1	
		34			NA[c]	4.7	
$FDAM_2$	NA[c]	9.5	MeOH	300	11.6	8.1	[16]
		34			11.6	4.9	
		9.5	CH_2Cl_2	300	12.3	9.6	
		34			11.3	6.7	
		9.5	$CHCl_3$	300	11.0	8.6	
		34			10.0	5.6	
		9.5	CH_2ClCH_2Cl	300	10.5	6.0	
		34			10.3	4.3	
		9.5	CH_3CH_2OH	300	10.1	6.0	
		34			10.0	3.1	
		9.5	Tert-butanol	300	11.7	4.0	
		34			12.2	1.4	
$FDAM_3$	NA[c]	9.5	MeOH	300	11.1	8.3	[16]
		34			9.7	5.6	
		9.5	$CHCl_3$	300	9.9	8.4	
		34			9.6	6.0	
OX63D	1	9.5	H_2O : glycerol = 4:6	77	3334[b]	NA[c]	[15]
		95			5000[b]		
OX63D	NA[c]	9.5	MeOH	300	16.5	5.8	[16]
		34			15.6	1.8	
		9.5	H_2O	300	16.0	7.3	
		34			15.3	2.2	
		9.5	D_2O	300	16.1	7.6	
		34			16.1	2.0	
DBT	NA[c]	9.5	MeOH	300	14.9	5	[16]
		34			14.3	2.1	

FBA_3	NA[c]	9.5	MeOH	300	19.5	6.5	16
		34			19.2	3.6	
		9.5	$CHCl_3$	300	18.0	7.2	
		34			17.6	4.5	
FP_3	NA[c]	9.5	MeOH	300	23.0	5.0	16
		34			23.0	2.8	
		9.5	$CHCl_3$	300	26.4	4.5	
		34			25.7	2.3	
$FDME_3$	NA[c]	9.5	MeOH	300	12.2	8.5	16
		34			11.2	5.4	
		9.5	$CHCl_3$	300	11.4	9.1	
		34			11.2	5.4	
BDPA	0.0007	9.5	Toluene	Ambient temperature	12[b]	9.8[b]	17
DPPH	0.012	9.5	Toluene	Ambient temperature	2.0[b]	1.3[b]	17
Galvinoxyl	0.0028	9.5	Toluene	Ambient temperature	2.8[b]	2.1[b]	17
Thianthrene	< 0.5	9.5	TFA	Ambient temperature	0.4[b]	0.4[b]	17
mCTPO	0.25	9.5	H_2O	Ambient temperature	0.53	0.67	17
PDT	0.25	9.5	H_2O	Ambient temperature	0.56	0.59	17
2,5-DTBSQ	0.3	9.5	Ethanol	Ambient temperature	7.8[b]	3.2[b]	6
2,6-DTBSQ	0.3	9.5	Ethanol	Ambient temperature	6.67[b]	NA[c]	
TMBSQ	0.3	9.5	Ethanol	Ambient temperature	5.56[b]		
TEMPO	1.0	9.5	H_2O: glycerol = 1:1	295[b]	2.00[b]	NA[c]	18
Tempone	0.3	9.5	H_2O: glycerol = 1:1	100	100[b]	5[b]	19
Tempol	3	9.5	Sucrose octaacetate	298[b]	19.95[b]	NA[c]	20
DTBN	3	9.5	Sucrose octaacetate	250[b]	5.6[b]	0.40[b]	
TEIO	3	9.5	Sucrose octaacetate	300[b]	25.12[b]	0.63[b]	
TMIO	3	9.5	Sucrose octaacetate	300[b]	NA[c]	1.26[b]	
TPHIO	3	9.5	Sucrose octaacetate	298[b]	56.23[b]	2.51[b]	
CTPO	3	9.5	Sucrose octaacetate	273[b]	15.85[b]	1.58	
tBuPyrr	3	9.5	Sucrose octaacetate	273[b]	NA[c]	0.63	
PCTM	0.2-0.5	9.5	Toluene : $CHCl_3$ = 4:1	298	10[b]	NA[c]	21
TCSQ	0.2-0.5	9.5	Triacetin : HMPA = 2:1	298	10[b]		
DDBSQ	0.2-0.5	9.5	H_2O : glycerol = 1:1	298	31.63[b]		
TTBP	0.53	9.1	H_2O : glycerol = 1:1	298	10[b]	NA[c]	22
THSQ	0.5	9.5	Ethanol : glycerol = 4:1	298	31.63[b]	NA[c]	23
2,5-TASQ	0.5	9.5	Ethanol : glycerol = 4:1	298	10[b]		
2,5-PSQ	0.5	9.5	Ethanol : glycerol = 4:1	298	10[b]		
PTTF	powder	NA[c]	NA[c]	300[b]	1[b]	0.5[b]	24
PtTTFtt	0.05	9.5	DCM	298	1.44[b]	0.34[b]	25
$(C_6F_5)_2B(O_2C_{14}H_8)$	0.1	9.5	Toluene : CH_2Cl_2 = 9:1	100	4600	2.6	26
BTI-xy	0.2	9.5	DMF : benzene = 1:1	10	6000[b]	1.3[b]	27
BTR-C_3	1	9.5	2-Methyltetrahydrofuran	5	1098	6.8	28
				110	23	2.8	
PDA	NA[c]	9.5	powder	5	46900	0.77	29
hydroxyl-DICPO	NA[c]	9.5	H_2O : glycerol = 1:1	100	400[b]	3.2[b]	30
oxo-DICPO	NA[c]	9.5	H_2O : glycerol = 1:1	100	400[b]	3.2[b]	
IA-DZD	NA[c]	35	H_2O : glycerol = 1:1	80	580	2.7	31
NO-1	NA[c]	9.5	Dried trehalose	Room temperature	12	0.735	32
NO-2					30	0.730	
NO-3a					17	0.750	

NO-3b					17	0.730	
NO-3c					21	0.8	
NO-3d					22	0.630	
NO-4a					18	0.680	
NO-4b					14	0.650	
NO-5a					18	0.640	
NO-5b					16	0.740	
NO-6a					23	0.655	
NO-6b					16	0.730	
NO-7a	NA[c]	9.5	Trehalose : sucrose = 9:1	Room temperature	NA[c]	0.50[b]	33
NO-7b						0.71[b]	
MTSL						0.34[b]	
NO-8a	NA[c]		Trehalose : sucrose = 9:1	295[b]	10[b]	1[b]	34
NO-8b	NA[c]		Trehalose :sucrose = 9:1	295[b]	10[b]	1[b]	
MTSSL	NA[c]	9.5	H_2O : glycerol = 1:1	240[b]	10[b]	0.1[b]	35
				100[b]	400[b]	1[b]	
Spiro-TOAC	NA[c]	9.5	H2O : glycerol = 1:1	240	NA[c]	0.1[b]	
				100		3.2[b]	
Spiro-IA	NA[c]	9.5	H_2O : glycerol = 1:1	100	NA[c]	3.16[b]	36
5-SASL	NA[c]	2.54	DMPC	300	1.34	NA[c]	37
		3.45			2.06		
		9.2			5.33		
		18.5			6.98		
		34.6			8.41		
12-SASL	NA[c]	2.54	DMPC	300	1.18	NA[c]	37
		3.45			1.67		
		9.2			4.41		
		18.5			5.81		
		34.6			6.11		
16-SASL	NA[c]	2.54	DMPC	300	0.69	NA[c]	37
		3.45			0.92		
		9.2			2.52		
		18.5			3.46		
		34.6			3.69		
NIT-polyphenylene	NA[c]	9.4	Powder	300[b]	1.43[b]	0.6[b]	38
NIT-GNRs					1.43[b]	0.2[b]	
GNRs-1	NA[c]	9.8	Powder	Room temperature	1[b]	0.3[b]	39
				5	100[b]	NA[c]	
			Toluene	5	5000[b]	2[b]	
			d-Toluene	5	10000[b]	NA[c]	
			CS_2	80[b]	NA[c]	100[b]	
GNRs-2	NA[c]	9.8	d-Toluene	15[b]	NA[c]	10[b]	39
			CS_2	10[b]		20[b]	
GNRs-3	NA[c]	9.4	Powder	10[b]	NA[c]	1[b]	40
	2±0.5		Toluene	300[b]	100[b]	6[b]	
	2±0.5		d-Toluene		83[b]	6[b]	
	2±0.5		CS_2		83[b]	7[b]	
	2±0.5		d_{14}OTP		1000[b]	6[b]	
GNRs-4	NA[c]	9.4	Powder	10[b]	NA[c]	0.2[b]	40
	2±0.5		Toluene	300[b]	125[b]	4[b]	
	2±0.5		d-Toluene		100[b]	3[b]	

	2±0.5		CS_2		100[b]	4[b]	
	2±0.5		d_{14}OTP		1000[b]	2[b]	
GNRs-5	NA[c]	9.4	Powder	10[b]	NA[c]	0.1[b]	40
	2±0.5		Toluene	300[b]	91[b]	5[b]	
	2±0.5		d-Toluene		250[b]	5[b]	
	2±0.5		CS_2		67[b]	5[b]	
	2±0.5		d_{14}OTP		1000[b]	3[b]	
NO2Ph-SWCNTs	NA[c]	9.5	d-Toluene	5	13000	1.2	41
D3CM	NA[c]	9.26	Powder	100[b]	800[b]	1[b]	42
				298[b]	20[b]	1[b]	
	0.1		d^8-Toluene	100[b]	1000[b]	4[b]	
3CM	NA[c]		Powder	100[b]	600[b]	0.7[b]	
				298[b]	15[b]	0.7[b]	
	0.1		d^8-Toluene	100[b]	1000[b]	2[b]	
D4CM	NA[c]		Powder	100[b]	300[b]	0.8[b]	
				298[b]	60[b]	0.6[b]	
	0.1		d^8-Toluene	100[b]	800[b]	4[b]	
4CM	NA[c]		Powder	100[b]	200[b]	0.2[b]	
	0.1		d^8-Toluene	100[b]	1000[b]	1[b]	

[a]Abbreviations are consistent with those in Figure S1-4; [b]value estimated from a figure in the reference; [c]not available.

Table S3. T_1 and T_m of stable organic radical qubits integrated in solid-state systems

Radical[a]	Molar percentage	Frequency / GHz	Temperature / K	T_1 / μs	T_m / μs	Reference
C_{50}-LA_{90}	1%[e]	9.73	30	2102	0.186	43
		9.65	298	25.02	0.148	
C_{50}-LA_{140}	0.7%[e]	9.73	30	3522	0.300	
		9.65	298	29.62	0.213	
C_{50}-LA_{400}	0.4%[e]	9.73	30	5173	0.377	
		9.65	298	29.23	0.318	
MgHOTP	0.66%	9.4	296	10.55	0.153	44
			296	21.61[b]	0.202[b]	
TAPPy-NDI	0.01%	9.4	100	790	1.26	45
			296	30.2	0.49	
	0.11%		100	333	0.727	
			296	11.8	0.484	
	2.1%		100	357	0.702	
			296	15	0.397	
	8.2%		100	257	0.448	
			296	11	0.283	
	15%		100	92.7	0.216	
			296	7.7	0.108	
	32%		100	30.6	0.166	
			296	1.68	0.150	
Ni-HATI_iPr	1%	9.7	100	3[c]	0.09[c]	46
Ni-HATI_vPr	0.3%	9.7	50	8[c]	0.08[c]	
Ni-HATI_nPr	0.4%	9.7	100	2[c]	0.07[c]	
PTCM-Film	0.1%	9.26	100	150[c]	1.5[c]	42
			298	35.6	1.08	
TEMPO SAM	N/A[d]	9.47	10	9200	13.53	47
BTEV-BTR	1%	9	80	386	4.39	48
			293	36	2.30	
	5%		293	29	1.73	
	10%		293	26	1.43	
	20%		80	75	1.86	
			293	20	0.98	

[a]Abbreviations are consistent with those in corresponding references; [b]MgHOTP soaked in THF; [c]value estimated from a figure in the reference; [d]not available; [e]value estimated from the synthetic condition.

References

1. Eaton, S.S., Eaton, G.R. (2018) Relaxation mechanisms. In EPR Spectroscopy: Fundamentals and Methods, Goldfarb, D., Stoll, S., ed. (Wiley), pp. 175–192.

2. Eaton, S.S., Eaton, G.R. (2000) Relaxation times of organic radicals and transition metal ions. In Distance Measurements in Biological Systems by EPR, Berliner, L. J., Eaton, G.R., Eaton, S.S., ed. (Kluwer Academic/Plenum Publishers), pp. 29–154.

3. Mirzoyan, R., Kazmierczak, N.P., Hadt, R.G. (2021). Deconvolving contributions to decoherence in molecular electron spin qubits: a dynamic ligand field approach. Chem. Eur. J. **27**: 9482–9494. DOI: 10.1002/chem.202100845.

4. Bhattacharyya, R., Chakraborty, I., Chakrabarti, A., et al. (2020). Recent studies on accurate measurements of NMR transverse relaxation times. Annu. Rep. NMR Spectrosc. **99**: 57–77. DOI: 10.1016/bs.arnmr.2019.09.001

5. Atzori, M., Sessoli, R. (2019). The second quantum revolution: role and challenges of molecular chemistry. J. Am. Chem. Soc. **141**: 11339–11352. DOI: 10.1021/jacs.9b00984.

6. Elajaili, H.B., Biller, J.R., Eaton, S.S., et al. (2014). Frequency dependence of electron spin–lattice relaxation for semiquinones in alcohol solutions. J. Magn. Reson. **247**: 81–87. DOI: 10.1016/j.jmr.2014.08.014.

7. Biller, J.R., Meyer, V.M., Elajaili, H., et al. (2012). Frequency dependence of electron spin relaxation times in aqueous solution for a nitronyl nitroxide radical and perdeuterated-tempone between 250 MHz and 34 GHz. J. Magn. Reson. **225**: 52–57. DOI: 10.1016/j.jmr.2012.10.002.

8. Biller, J.R., Elajaili, H., Meyer, V., et al. (2013). Electron spin–lattice relaxation mechanisms of rapidly-tumbling nitroxide radicals. J. Magn. Reson. **236**: 47–56. DOI: 10.1016/j.jmr.2013.08.006.

9. Shi, Y., Quine, R.W., Rinard, G.A., et al. (2017). Triarylmethyl radical: EPR signal to noise at frequencies between 250 MHz and 1.5 GHz and dependence of relaxation on radical and salt concentration and on frequency. Z. Für Phys. Chem. **231**: 923–937. DOI: 10.1515/zpch-2016-0813.

10. Ghim, B.T., Du, J.-L., Pfenninger, S., et al. (1996). Multifrequency electron paramagnetic resonance of irradiated L-alanine. Appl. Radiat. Isot. **47**: 1235–1239. DOI: 10.1016/s0969-8043(96)00037-1.

11. Kevan, L., Narayana, P.A. (1979) Disordered matrices. In Multiple Electron Resonance Spectroscopy, Dorio, M.M., Freed, J.H., ed. (Plenum Press), pp. 229–260.

12. Bowman, M.K., Norris, J.R. (1982). Cross relaxation of free radicals in partially ordered solids. J. Phys. Chem. **86**: 3385–3390. DOI: 10.1021/j100214a024.

13. Fielding, A.J., Carl, P.J., Eaton, G.R., et al. (2005). Multifrequency EPR of four triarylmethyl radicals. Appl. Magn. Reson. **28**: 231–238. DOI: 10.1007/BF03166758.

14. Yong, L., Harbridge, J., Quine, R.W., et al. (2001). Electron spin relaxation of triarylmethyl radicals in fluid solution. J. Magn. Reson. **152**: 156–161. DOI: 10.1006/jmre.2001.2379.

15. Chen, H., Maryasov, A.G., Rogozhnikova, O. Y., et al. (2016). Electron spin dynamics and spin–lattice relaxation of trityl radicals in frozen solutions. Phys. Chem. Chem. Phys. **18**: 24954–24965. DOI: 10.1039/c6cp02649d.

16. Kuzhelev, A.A., Trukhin, D.V., Krumkacheva, O.A., et al. (2015). Room-temperature electron spin relaxation of triarylmethyl radicals at the X- and Q- bands. J. Phys. Chem. B **119**: 13630–13640. DOI: 10.1021/acs.jpcb.5b03027.

17. Meyer, V., Eaton, S.S., Eaton, G.R. (2014). X-band electron spin relaxation times for four aromatic radicals in fluid solution and comparison with other organic radicals. Appl. Magn. Reson. **45**: 993–1007. DOI: 10.1007/s00723-014-0579-6.

18. Sato, H., Bottle, S.E., Blinco, J.P., et al. (2008). Electron spin–lattice relaxation of nitroxyl radicals in temperature ranges that span glassy solutions to low-viscosity liquids. J. Magn. Reson. **191**: 66–77. DOI: 10.1016/j.jmr.2007.12.003.

19. Nakagawa, K., Candelaria, M.B., Chik, W.W.C., et al. (1992). Electron-spin relaxation times of chromium(V). J. Magn. Reson. **98**: 81–91. DOI: 10.1016/0022-2364(92)90111-J.

20. Sato, H., Kathirvelu, V., Fielding, A., et al. (2007). Impact of molecular size on electron spin relaxation rates of nitroxyl radicals in glassy solvents between 100 and 300 K. Mol. Phys. **105**: 2137–2151. DOI: 10.1080/00268970701724966.

21. Kathirvelu, V., Eaton, G.R., Eaton, S.S. (2009). Impact of chlorine substitution on spin–lattice relaxation of triarylmethyl and 1,4-benzosemiquinone radicals in glass-forming solvents between 25 and 295 K. Appl. Magn. Reson. **37**: 649. DOI: 10.1007/s00723-009-0086-3.

22. Harbridge, J.R., Eaton, S.S., Eaton, G.R. (2003). Electron spin-lattice relaxation processes of radicals in irradiated crystalline organic compounds. J. Phys. Chem. **107**: 598–610. DOI: 10.1021/jp021504h.

23. Kathirvelu, V., Sato, H., Eaton, S.S., et al. (2009). Electron spin relaxation rates for semiquinones between 25 and 295 K in glass-forming solvents. J. Magn. Reson. **198**: 111–120. DOI: 10.1016/j.jmr.2009.01.026.

24. Krinichnyi, V.I., Pelekh, A.E., Roth, H.-K., et al. (1993). Spin relaxation studies on conducting poly(tetrathiafulvalene). Appl. Magn. Reson. **4**: 345–356. DOI: 10.1007/BF03162508.

25. McNamara, L., Zhou, A., Rajh, T., et al. (2023). Realizing solution-phase room temperature quantum coherence in a tetrathiafulvalene-based diradicaloid complex. Cell Rep. Phys. Sci. **4**: 101693. DOI: 10.1016/j.xcrp.2023.101693.

26. Eaton, S.S., Huber, K., Elajaili, H., et al. (2017). Electron spin relaxation of a boron-containing heterocyclic radical. J. Magn. Reson. **276**: 7–13. DOI: 10.1016/j.jmr.2016.12.013.

27. Koyama, S., Sato, K., Yamashita, M., et al. (2023). Observation of slow magnetic relaxation phenomena in spatially isolated π-radical ions. Phys. Chem. Chem. Phys. **25**: 5459–5467. DOI: 10.1039/d2cp06026d.

28. Boudalis, A.K., Constantinides, C.P., Chrysochos, N., et al. (2023). Deciphering the ground state of a C_3-symmetrical Blatter-type triradical by CW and pulse EPR spectroscopy. J. Magn. Reson. **349**: 107406. DOI: 10.1016/j.jmr.2023.107406.

29. Tadyszak, K., Mrówczyński, R., Carmieli, R. (2021). Electron spin relaxation studies of polydopamine radicals. J. Phys. Chem. B **125**: 841–849. DOI: 10.1021/acs.jpcb.0c10485.

30. Kathirvelu, V., Smith, C., Parks, C., et al. (2009). Relaxation rates for spirocyclohexyl nitroxyl radicals are suitable for interspin distance measurements at temperatures up to about 125 K. Chem. Commun., 454–456. DOI: 10.1039/b817758a.

31. Yang, Z., Stein, R.A., Ngendahimana, T., et al. (2020). Supramolecular approach to electron paramagnetic resonance distance measurement of spin-labeled proteins. J. Phys. Chem. B **124**: 3291–3299. DOI: 10.1021/acs.jpcb.0c00743.

32. Kuzhelev, A.A., Strizhakov, R.K., Krumkacheva, O.A., et al. (2016). Room-temperature electron spin relaxation of nitroxides immobilized in trehalose: effect of substituents adjacent to no-group. J. Magn. Reson. **266**: 1–7. DOI: 10.1016/j.jmr.2016.02.014.

33. Huang, S., Pink, M., Ngendahimana, T., et al. (2021). Bis-spiro-oxetane and bis-spiro-tetrahydrofuran pyrroline nitroxide radicals: synthesis and electron spin relaxation studies. J. Org. Chem. **86**: 13636–13643. DOI: 10.1021/acs.joc.1c01670.

34. Huang, S., Paletta, J.T., Elajaili, H., et al. (2017). Synthesis and electron spin relaxation of tetracarboxylate pyrroline nitroxides. J. Org. Chem. **82**: 1538–1544. DOI: 10.1021/acs.joc.6b02737.

35. Rajca, A., Kathirvelu, V., Roy, S.K., et al. (2010). A spirocyclohexyl nitroxide amino acid spin label for pulsed EPR spectroscopy distance measurements. Chem. Eur. J. **16**: 5778–5782. DOI: 10.1002/chem.200903102.

36. Meyer, V., Swanson, M.A., Clouston, L.J., et al. (2015). Room-Temperature distance measurements of immobilized spin-labeled protein by DEER/PELDOR. Biophys. J. **108**: 1213–1219. DOI: 10.1016/j.bpj.2015.01.015.

37. Hyde, J.S., Yin, J.-J., Subczynski, W.K., et al. (2004). Spin-label EPR T_1 values using saturation recovery from 2 to 35 GHz. J. Phys. Chem. B **108**: 9524–9529. DOI: 10.1021/jp036329z.

38. Slota, M., Keerthi, A., Myers, W.K., et al. (2018). Magnetic edge states and coherent manipulation of graphene nanoribbons. Nature **557**: 691–695. DOI: 10.1038/s41586-018-0154-7.

39. Lombardi, F., Lodi, A., Ma, J., et al. (2019). Quantum units from the topological engineering of molecular graphenoids. Science **366**: 1107–1110. DOI: 10.1126/science.aay7203.

40. Lombardi, F., Ma, J., Alexandropoulos, D.I., et al. (2021). Synthetic tuning of the quantum properties of open-shell radicaloids. Chem **7**: 1363–1378. DOI: 10.1016/j.chempr.2021.03.024.

44. Chen, J.-S., Trerayapiwat, K.J., Sun, L., et al. (2023). Long-lived electronic spin qubits in single-walled carbon nanotubes. Nat. Commun. **14**: 848. DOI: 10.1038/s41467-023-36031-z.

42. Dai, Y., Dong, B., Kao, Y., et al. (2018). Chemical modification toward long spin lifetimes in organic conjugated radicals. ChemPhysChem **19**: 2972–2977. DOI: 10.1002/cphc.201800742

43. Hou, L., Zhang, Y., Zhang, Y., et al. (2024). Tunable quantum coherence of luminescent molecular spins organized via block copolymer self-assembly. Adv. Quantum Technol. 2400064. DOI: 10.1002/qute.202400064

44. Sun, L., Yang, L., Dou, J.-H., et al. (2022). Room-temperature quantitative quantum sensing of lithium ions with a radical-embedded metal–organic framework. J. Am. Chem. Soc. **144**: 19008–19016. DOI: 10.1021/jacs.2c07692.

45. Oanta, A.K., Collins, K.A., Evans, A.M., et al. (2023). Electronic spin qubit candidates arrayed within layered two-dimensional polymers. J. Am. Chem. Soc. **145**: 689–696. DOI: 10.1021/jacs.2c11784.

46. Lu, Y., Hu, Z., Petkov, P., et al. (2024). Tunable charge transport and spin dynamics in two-dimensional conjugated metal–organic frameworks. J. Am. Chem. Soc. **146**: 2574–2582. DOI: 10.1021/jacs.3c11172.

47. Tesi, L., Stemmler, F., Winkler, M., et al. (2023). Modular approach to creating functionalized surface arrays of molecular qubits. Adv. Mater. **35**:2208998.

48. Poryvaev, A.S., Gjuzi, E., Polyukhov, D.M., et al. (2021). Blatter-radical-grafted mesoporous silica as prospective nanoplatform for spin manipulation at ambient conditions. Angew. Chem. Int. Ed. **60**: 8683–8688. DOI: 10.1002/anie.202015058.